Available online at www.sciencedirect.com

ScienceDirect

Publishing Services by Elsevier

International Journal of Naval Architecture and Ocean Engineering 9 (2017) 77–99

http://www.journals.elsevier.com/international-journal-of-naval-architecture-and-ocean-engineering/

Numerical hydrodynamic analysis of an offshore stationary–floating oscillating water column–wave energy converter using CFD

Ahmed Elhanafi*, Alan Fleming, Gregor Macfarlane, Zhi Leong

National Centre for Maritime Engineering and Hydrodynamics, Australian Maritime College, University of Tasmania, Launceston, Tasmania 7250, Australia

Received 21 March 2016; revised 9 July 2016; accepted 9 August 2016

Available online 1 October 2016

Abstract

Offshore oscillating water columns (OWC) represent one of the most promising forms of wave energy converters. The hydrodynamic performance of such converters heavily depends on their interactions with ocean waves; therefore, understanding these interactions is essential. In this paper, a fully nonlinear 2D computational fluid dynamics (CFD) model based on RANS equations and VOF surface capturing scheme is implemented to carry out wave energy balance analyses for an offshore OWC. The numerical model is well validated against published physical measurements including; chamber differential air pressure, chamber water level oscillation and vertical velocity, overall wave energy extraction efficiency, reflected and transmitted waves, velocity and vorticity fields (PIV measurements). Following the successful validation work, an extensive campaign of numerical tests is performed to quantify the relevance of three design parameters, namely incoming wavelength, wave height and turbine damping to the device hydrodynamic performance and wave energy conversion process. All of the three investigated parameters show important effects on the wave–pneumatic energy conversion chain. In addition, the flow field around the chamber's front wall indicates areas of energy losses by stronger vortices generation than the rear wall.

Keywords: Offshore oscillating water column; OWC; Wave energy; Energy balance; Numerical wave tank

1. Introduction

Wave energy is one of the most promising renewable energy resources and research is being conducted worldwide. There is a large number of invented techniques for wave energy conversion which can be categorised by deployment location (shoreline, nearshore and offshore), type (attenuator, point absorber and terminator) and mode of operation (submerged pressure differential, oscillating wave surge converter, oscillating water column and overtopping device) (Drew et al., 2009).

The Oscillating Water Column (OWC) is a wave energy extraction device that is based on wave to air energy conversion by driving an oscillating column in a chamber open to the sea. The air energy is extracted by means of a bi–directional air turbine connected to the chamber. As the water level oscillates up and down inside the chamber, the air inside it is compressed and decompressed, respectively. In turn, this process generates mechanical energy through a reversible flow between the atmosphere and the chamber utilizing an air turbine that rotates in the same direction regardless of the airflow direction. Different from other Wave Energy Converters (WEC), OWCs are not only one of the simplest devices from an operational point of view, but also having no moving parts underwater provides lesser and easier maintenance works. OWCs can be deployed as fixed structures at the shoreline or nearshore, or integrated in breakwaters and floating structures (Falcão and Henriques, 2015).

Investigating the hydrodynamic performance of OWCs has been studied analytically, experimentally, numerically or a combination of the aforementioned. A theoretical model of the

* Corresponding author.
E-mail address: Ahmed.Elhanafi@utas.edu.au (A. Elhanafi).

Peer review under responsibility of Society of Naval Architects of Korea.

http://dx.doi.org/10.1016/j.ijnaoe.2016.08.002

hydrodynamics for a fixed OWC device was developed by Evans (1978). Ignoring the spatial variation, Evans assumed a rigid weightless piston motion for the chamber's internal free surface of a small width relative to the incident wavelength, which allowed the application of the oscillating body theory. Falcão and Sarmento (1980), Evans (1982) and Falnes and McIver (1985) improved the rigid–body approach of an OWC via allowing the increase in pressure at the free surface as well as providing the possibility of a non–plane surface.

With the aim of validating the oscillating surface pressure theory proposed by Sarmento and Falcão (1985) in OWCs, Sarmento (1992) conducted a set of wave flume experiments with regular waves of very small steepness under linear, as well as quadratic, power take–off (PTO) simulated by either filters or orifice plate, accordingly. Hong Hong et al. (2007) performed a 2D experiment concentrating on the effects of several shape parameters of OWC chamber in wave energy absorbing capability. Morris-Thomas et al. (2007) performed experiments in a wave flume to investigate the influence of the chamber's front wall thickness, shape and draught under various wave parameters on the hydrodynamic efficiency of a shore–based OWC device.

Generally, numerical models can be divided into two categories; the first category is based on applying potential flow theory, which is usually solved with a boundary element method (BEM). Extensive review of potential flow models can be found in Baudry et al. (2013). The second category, which is applied in the present study, is based on Reynolds–averaged Navier–Stokes (RANS) equations, which provides more advantages in overcoming the potential flow weaknesses in handling problems that involve strong nonlinearity, dispersion, wave breaking, complex viscous, turbulence and vortex shedding. This method is widely used by several researchers; examples that are most relevant to the present study include Zhang et al. (2012) who developed, validated and studied the impact the geometrical parameters have on a shore–based OWC efficiency curve using a 2D two–phase numerical wave tank based on a level–set immersed boundary method. They reported a reasonable agreement with experimental data measured by Morris-Thomas et al. (2007) for the device hydrodynamic efficiency with a slight over–prediction attributed to the complex pressure changes in the chamber around resonance. Additional parameters such as pressure variation, free surface elevation inside the chamber and flow field were presented and discussed, but without comparison to experimental data. Teixeira et al. (2013) implemented a numerical model (Fluinco) based on the two–step semi–implicit Taylor–Galerkin method to simulate a fixed OWC device subjected to regular waves. After validating their model against numerical results from the commercial CFD code Fluent, they investigated the effects of the chamber geometry including the front wall depth, chamber length, chamber height and the turbine characteristic relation that provide the best device performance. Luo et al. (2014) implemented a 2D numerical model using a commercial CFD code (Fluent) to investigate the effect of wave nonlinearity on the capture efficiency of an onshore OWC device. López et al. (2014, 2016) studied the importance of different turbine damping coefficients on the performance of an onshore OWC device under regular and irregular waves to determine the optimum turbine–induced damping on an OWC device using a 2D commercial CFD model (Star–CCM+). Kamath et al. (2015a, 2015b) utilized a 2D open–source CFD model (REEF3D) to simulate and study the interaction of a fixed shore–based OWC with regular waves of different wavelengths and steepness, and also investigated the response of the OWC under different damping values from the PTO device.

Quantifying the energy losses inside OWCs has not been studied extensively in comparison with the considerable research effort focused on the overall hydrodynamic performance and geometry optimization of onshore OWCs. Always in such research, there is a part of the incoming wave energy that is assumed to be lost inside the OWC system; however, only a few researchers have paid more attention to either visualizing and/or quantifying such losses. Only via visualizing the flow behaviour in a shoreline OWC, Müller and Whittaker (1995) highlighted different energy loss mechanisms. Tseng et al. (2000) experimentally estimated about 33%–68% energy losses throughout the energy conversion chain for a multi–resonant cylindrical caisson. Similarly, Mendes and Monteiro (2007) carried out a series of wave tank experiments on a shoreline OWC under regular waves. In addition to studying the energy conversion chain and estimating the energy losses, they visualized the flow inside the OWC using a sequence of video–frames to discover the energy dissipation physics.

Furthermore, by utilizing advanced measurement techniques such as particle imaging velocimetry (PIV), a detailed flow field picture can be obtained. For instance, using PIV, Morrison (1995) calculated the kinetic energy and viscous dissipation rates in a shore–based OWC. Graw et al. (2000) studied the impact of an onshore OWC underwater geometry such as the front lip shape and its inclination on the energy losses in the vicinity of the lip over four wave frequencies. They concluded that at low frequencies with the cornered lip shape, the mean energy losses over one cycle (mean dissipation divided by the mean power) may be as much as 15%. Within the wave energy balance framework, Fleming et al. (2011, 2012a, 2012b and 2013) utilized flow field measurements using PIV in a forward facing bent duct OWC with a phase–averaging technique to perform detailed energy balance analyses considering different energy sources, stores and sinks components. López et al. (2015) applied Reynolds decomposition technique to estimate the turbulent kinetic energy in a shore–based OWC by resolving the velocity fluctuations from PIV measurement. Using this methodology, they investigated the relevance of different wave conditions, PTO pneumatic damping and change in tidal level on the OWC hydrodynamic performance. With respect to numerical modelling, Elhanafi et al. (2016b) developed a 2D numerical model based on RANS–VOF with validation against experimental results including PIV data. Building on the achieved good agreement, they applied their model to further investigate the impact of increasing the incident wave amplitude and

turbine damping on the energy conversion process in a fixed bottom–standing OWC device.

All of the abovementioned publications consider the common fixed onshore or nearshore types of OWC devices where the chamber rear wall is resting on the shoreline or extending to the seabed, respectively. Thus, no wave energy can be transmitted behind these OWC structures. In contrast, offshore OWCs are typically floating structures that allow ocean waves to pass around and underneath the device walls; accordingly, the incoming wave energy decomposition will consider an additional sink component for the transmitted wave energy. Subsequently, this will change the wave energy balance model, and affect the absorbed energy, extracted energy and the design parameters. Research on assessing the offshore OWCs performance is limited in comparison with the shore–based OWCs. In this regard, He and Huang (2014) and He et al. (2012, 2013) experimentally studied a pile–supported and a floating rectangular breakwater with pneumatic damping, respectively. In their study, more attention was given for the shore protection objective through quantifying the relevance of different design parameters such as wave frequency, pneumatic damping and the device draught to the transmission, reflection, air pressure and loss coefficients. Energy dissipation was assumed to come from two sources: vortex shedding at the tips of the chamber walls and the pneumatic power. This assumption was properly given due to the high cost and risk associated with required instruments to visualize and evaluate these losses such as using PIV. Although air pressure coefficients describing the pressure fluctuation inside the OWC chamber were measured, no output power measurements were given, and only one wave height representing weakly nonlinear waves with a maximum steepness of 0.029 and 0.023 for the fixed and floating OWC, respectively. Within the potential flow theory and its abovementioned shortcomings, Hong et al. (2004) investigated the motion and the drift force of a free floating OWC in regular waves. Sheng et al. (2014) utilized experimental data to validate a potential flow solver (WAMIT) in simulating a floating cylindrical OWC. Recently, Iturrioz et al. (2014, 2015) developed and validated a CFD model based on RANS–VOF using open source code (IHFOAM) with flume tank experiments to study the hydrodynamics and pneumatics around a fixed detached OWC. Crema et al. (2015) experimentally investigated the pneumatic efficiency of an OWC to be installed on a floating platform. The OWC device has back and side walls extending deeply in the water to increase the water column oscillation by increasing wave reflection, and their study included different geometrical parameters and both regular and irregular waves under different pneumatic damping. Simonetti et al. (2015) presented the numerical settings of an open source CFD code (OpenFOAM) and validation results against physical measurements of a similar OWC device tested by Crema et al. (2015). However, none of these studies investigate the impact of the wave height and the PTO damping on the offshore OWC hydrodynamic efficiency and wave energy conversion process through a detailed wave energy balance analysis, which is a part of the added values of the present work.

Providing a better understanding of the hydrodynamic performance of offshore OWCs through a detailed wave energy balance analysis is the driving force behind the present study. In this way, the present paper utilizes a 2D numerical model based on RANS equations solver with a VOF surface capturing scheme introduced by Hirt and Nichols (1981) to investigate the hydrodynamics of a stationary–floating offshore OWC device. With the CFD model, the OWC hydrodynamic performance is deeply investigated via a series of numerical wave energy balance analyses under different design parameters such as incoming wave height and frequency and PTO damping. The analysis includes the variation of the free surface, air pressure and airflow rate inside the chamber and the incident wave energy decomposition into reflected, transmitted, absorbed, extracted, stored and losses. Additionally, a detailed flow field analysis is conducted to uncover the energy losses mechanism through the vortex generation and dissipation processes.

2. Numerical model

2.1. Governing equations and numerical settings

In the present study, the numerical model assumes incompressible flow in the OWC chamber considering that air compressibility effect is negligible in the small model scale used herein. The flow motion of the incompressible fluid is described by the continuity and RANS equations. In RANS, the instantaneous velocity and pressure fields in the Navier–Stokes equations are decomposed into mean and fluctuating components, and then time–averaged. This process results in additional unknowns called Reynolds stresses that need to be modelled. In this paper, the two–equation Shear Stress Transport (SST) $k-\omega$turbulence model is implemented to model the Reynolds stresses in order to mathematically close the problem. Star–CCM + code is utilised to solve the flow sets of equations. The numerical model settings are as follows, time modelling: implicit unsteady with second–order temporal discretization scheme, flow modelling: segregated flow model with second–order upwind scheme (the segregated flow solver controls the solution update for the segregated flow model according to the SIMPLE algorithm) and multiphase model: VOF with segregated VOF solver that controls the solution update for the phase volume fractions (i.e. solve the discretized volume–fraction conservation equation for each phase present in the flow) with second–-order convection (CD-Adapco, 2015).

2.2. Computational fluid domain

Ocean waves are the primary exciting source acting on offshore structures such as OWCs and therefore, accurate modelling of these waves is crucial for providing a good estimation of the hydrodynamic loads and predict the structure's response and performance (Elhanafi et al., 2016a). The computational domain considered herein is divided into three main regions namely: domain, free surface and OWC, as

illustrated in Fig. 1. Domain lengths with different damping zone lengths are studied in order to properly select the location of the OWC and wave probe array along the tank. This study revealed that an overall domain length of 10 L, where L is the considered wavelength (L) is sufficient for collecting eight wave periods up to a distance of 8 L without getting reflection (negligible) from outlet boundary assigned at the end of the wave–damping zone of 1 L in length. In Star–CCM + code (CD-Adapco, 2015), waves are damped by implementing the method of Choi and Yoon (2009) by adding a resistance term to the equation for the vertical velocity component. The tank width is set to only two cells (2D model), and the OWC model is placed at a distance of 6.5 L from the wave inlet boundary. Considering the water oscillation inside the OWC chamber as well as the partial standing waves envelope generation in front of the chamber, a free surface zone height of 3.0 times the wave height (H) is adapted. Based on the grid and time sensitivity studies carried out it is found that when a base grid cell size of 400 mm is applied for the domain zone and the cell aspect ratio at the free surface zone is kept less than 16 with at least 12 and 36 cells per wave height and wavelength respectively, accurate water waves of less than 1.5% wave height error can be generated. Also, with Second–order temporal discretization scheme with 1200 time steps per wave period (T) is selected, this error becomes less than 1.0% in comparison with the analytical input wave height. Additional surface refinement is applied with 6.25 mm and 0.78125 mm cell surface size for the OWC walls and the PTO slot opening, respectively. For all non–slip walls, a first cell height equivalent to $y+ \cong 1$ ($y+$ is a non-dimensional distance from the wall to the first cell, and obtained by multiplying this distance with the friction/shear velocity divided by the kinematic viscosity) is used with a growth rate of 1.5 and 10 prism layers. The initial conditions implemented in the present CFD model are set as: the water level is defined at the desired level (h), waves are prescribed by the velocity components at the wave velocity inlet boundary and fully generated throughout the whole domain until the OWC's front lip by specifying that point on the water level, the tank two sides are defined as symmetry plans and atmospheric pressures is defined at the top and end boundaries.

3. OWC energy conversion chain

It is paramount to get a good understanding of the impact of the environmental conditions in terms of incoming wave height and frequency together with the PTO pneumatic damping not only on the extracted energy but also on the different components included in the wave–pneumatic energy conversion chain. Therefore, the energy conversion chain proposed and applied for onshore–based OWCs (Elhanafi et al., 2016b; Mendes and Monteiro, 2007; Tseng et al., 2000) is extended in the present study to consider an additional sink for the energy transmitted underneath the device as given by Eq. (1) and described in Fig. 2 with the different performance assessment parameters/coefficients.

$$E_I = E_R + E_T + E_E + E_S + E_L \tag{1}$$

where E_I is the incident wave energy, E_R is the reflected energy, E_T is the transmitted energy, E_E is the extracted/pneumatic energy, E_S is the energy stored in OWC chamber's internal heave motion and E_L is the energy losses.

Using regular wave theory, the incident wave energy per unit width is defined as the product of the total (potential and kinetic) wave energy per unit ocean's surface area and the incident wavelength (L):

$$E_I = \frac{1}{2}\rho g A^2 L \left[\frac{J}{m}\right] \tag{2}$$

where A is the incoming wave amplitude, ρ is the water density and g is the gravitational acceleration.

Considering that all of the incident, reflected and transmitted energy are proportional to the square of the wave height, the wave reflection coefficient (C_R) is defined as the ratio between the reflected wave height (H_R) and the incident

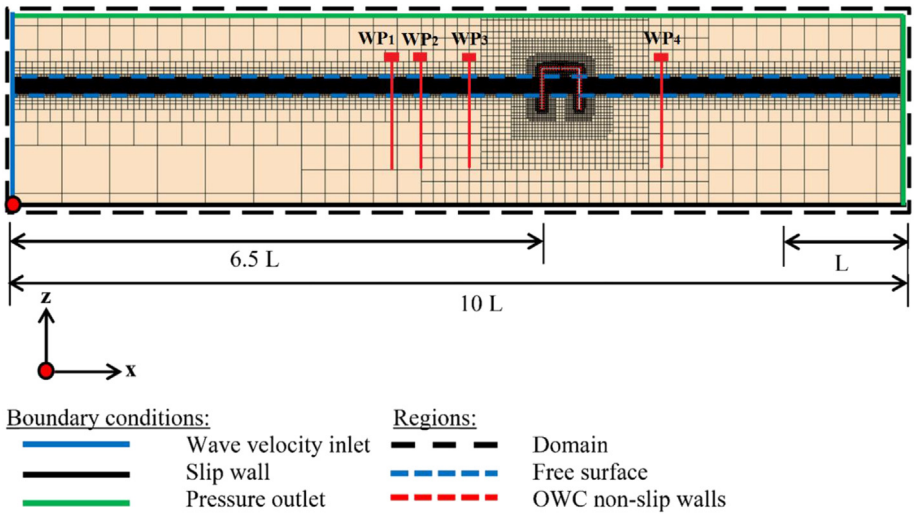

Fig. 1. Computational fluid domain (Not to scale).

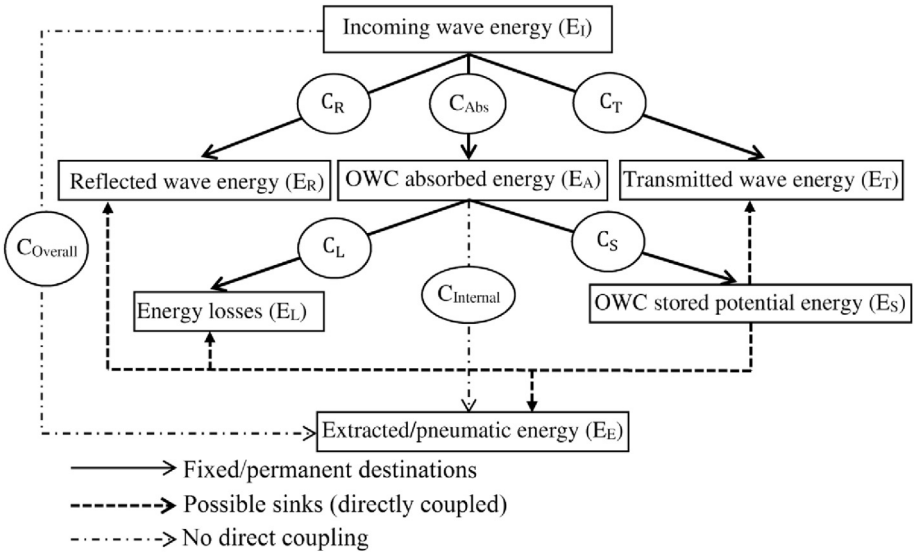

Fig. 2. Offshore stationary–floating OWC wave energy balance chart.

wave height (H), whereas the transmission coefficient (C_T) is given by the ratio of the transmitted wave height (H_T) measured behind the OWC structure to the incident wave height. Three numerical wave probes placed in front of the chamber sea wall are used to resolve the incident and reflected waves based on Mansard and Funke (1980) method. The spacing between the wave probes (shown in Fig. 1) were adjusted for each frequency according to the criteria specified by Mansard and Funke (1980), so that the spacing between WP_1 and WP_2 is L/10 and between WP_1 and WP_3 is L/4. Also, WP_3 is located at 0.75 L from the OWC front wall, which is more that 0.2 L as recommended by Goda and Suzuki (1976) in case of regular wave test. The transmitted wave height is measured at a distance of about one wavelength behind the OWC lee side, which is inside the tank area of free wave reflection (see Section 2.2).

While a part of the incoming wave energy is being reflected and transmitted as a result of the wave–OWC structure interactions, the rest is the energy absorbed by the OWC (E_A), which represents the maximum available energy to be extracted for electricity generation; and is given by:

$$E_A = E_I - E_R - E_T = E_I\left(1 - C_R^2 - C_T^2\right)\left[\frac{J}{m}\right] \tag{3}$$

The energy available at the turbine (extracted energy) (E_E) over one wave period is given by Eq. (4) as the time–integral of product of the instantaneous chamber's differential air pressure ($\Delta P(t)$) between the chamber interior and the exterior atmosphere and the airflow rate across the PTO ($q(t)$) (Elhanafi et al., 2016b; Tseng et al., 2000).

$$E_E = \int_0^T \Delta P(t)\cdot q(t)dt\left[\frac{J}{m}\right] \tag{4}$$

The energy stored in the OWC (E_S)represents the energy contained in the standing wave entrapped inside the chamber. This potential energy depends on the instantaneous oscillation of the chamber free surface (η) from its still water level, and is given by Eq. (5) per chamber's unit width (Elhanafi et al., 2016b). While the average value over a wave period is given by Eq. (6) (Elhanafi et al., 2016b; Mendes and Monteiro, 2007; Tseng et al., 2000) as a result of time–averaging of Eq. (5):

$$\grave{E}_s = \frac{\rho g \eta^2 b}{2}\left[\frac{J}{m}\right] \tag{5}$$

$$E_s = \frac{1}{T}\int_0^T \frac{\rho g \eta^2 b}{2} dt = \frac{\rho g H_w^2 b}{16}\left[\frac{J}{m}\right] \tag{6}$$

where b is the chamber length in the wave propagation direction and H_w is the height of the water column oscillations inside the OWC's chamber.

Considering the energy conservation principle in Eq. (1) and applying the energy balance chain shown in Fig. 2, the total losses in the OWC can be defined as the rest of the absorbed energy that has not been converted into pneumatic energy minus the energy stored in the water column oscillations. These losses (E_L) given in Eq. (7) can be attributed to different sources such as wave breaking, viscous, turbulence and vortex losses at chamber' lips and PTO.

$$E_L = E_A - E_E - E_S\left[\frac{J}{m}\right] \tag{7}$$

With estimating the different wave energy components together with the energy balance chain illustrated in Fig. 2, the OWC hydrodynamic performance is evaluated by analysing the energy balance coefficients summarized in Table 1.

In addition, to assess the OWC's overall power extraction efficiency, it is important to not only consider the incoming

wave height and length as in calculating the incoming energy (Eq. (2)), but also, the group velocity needs to be taken into account. Therefore, using regular wave theory, the incident wave energy flux (power) (P_I) per unit width is defined as the product of the incoming wave energy per unit ocean's surface area and the group velocity (C_g) (Dalrymple and Dean, 1991). Then, the OWC's overall power extraction efficiency ($\zeta_{Overall}$) is defined as in Eq. (10):

$$P_I = \frac{1}{2}\rho g A^2 C_g \left[\frac{W}{m}\right] \tag{8}$$

$$C_g = \begin{cases} \frac{\omega}{2k}\left(1+\frac{2kh}{\sinh(2kh)}\right) & \text{for intermediate water conditions}\left(\frac{L}{20}<h<\frac{L}{2}\right) \\ \frac{1}{2}\frac{L}{T} & \text{for deep water conditions}\left(h>\frac{L}{2}\right) \end{cases} \left[\frac{m}{s}\right] \tag{9}$$

where ω is the wave angular frequency, k is the wave number given by the dispersion relationship $\omega^2/g = k\tanh(kh)$ and h is the still water depth.

$$\zeta_{Overall} = \frac{P_E}{P_I}[-] \tag{10}$$

where P_E is the pneumatic extracted power, and is given by Eq. (11) as the time−average of Eq. (4) (Mendes and Monteiro, 2007):

$$P_E = \frac{1}{T}\int_0^T \Delta P(t)\cdot q(t)dt \left[\frac{W}{m}\right] \tag{11}$$

4. Experiments and validations

The numerical model used in the present study was previously validated in capturing the flow field (velocity and vorticity) inside an onshore OWC as well as monitoring the wave elevation along the numerical wave tank (Elhanafi et al., 2016b). Herein, additional two sets of experiments are used for further validating the numerical model. In the first validation, important parameters including chamber instantaneous differential air pressure (ΔP), chamber free surface elevation (η), chamber free surface vertical velocity (V) and overall system hydrodynamic efficiency ($\zeta_{Overall}$) are considered. The numerical results are compared against experimental measurements conducted by Morris-Thomas et al. (2007) (Case−B) and others numerical model results for the OWC model shown in Fig. 3.

As given in Eq. (11), both chamber's differential air pressure and airflow rate through the PTO are the two parameters required to evaluate the extracted pneumatic power. The differential pressure is numerically monitored by measuring the pressure at two points: one inside the chamber and another outside (on domain top boundary). A numerical array of different points inside the chamber at 1−20 mm from the back wall and 50−125 mm from the top wall have been tested, and there are no differences found for the positive pressure, while little variations are observed for the negative values. Airflow rate can simply be monitored numerically by measuring the air volume flow rate through the PTO via performing surface integral to the air's normal velocity or dividing the monitored

Table 1
Offshore OWC energy balance coefficients.

Wave energy balance coefficient	Description
Overall pneumatic energy extraction ($C_{Overall}$)	E_E/E_I
Reflected energy (C_R^2)	$(H_R/H)^2$
Transmitted energy (C_T^2)	$(H_T/H)^2$
OWC energy absorption (C_{Abs})	E_A/E_I
OWC internal energy extraction ($C_{Internal}$)	E_E/E_A
Energy losses (C_L)	E_L/E_A
OWC stored energy (C_S)	E_s/E_A

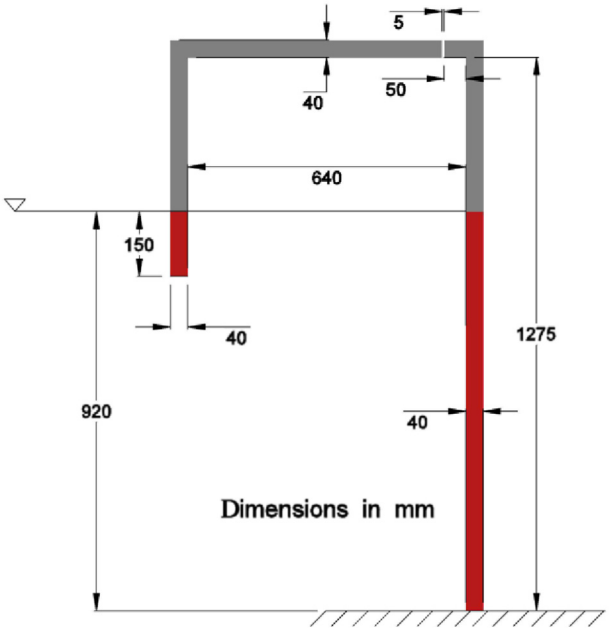

Fig. 3. Schematic of the OWC device (Case−B) tested by Morris-Thomas et al. (2007).

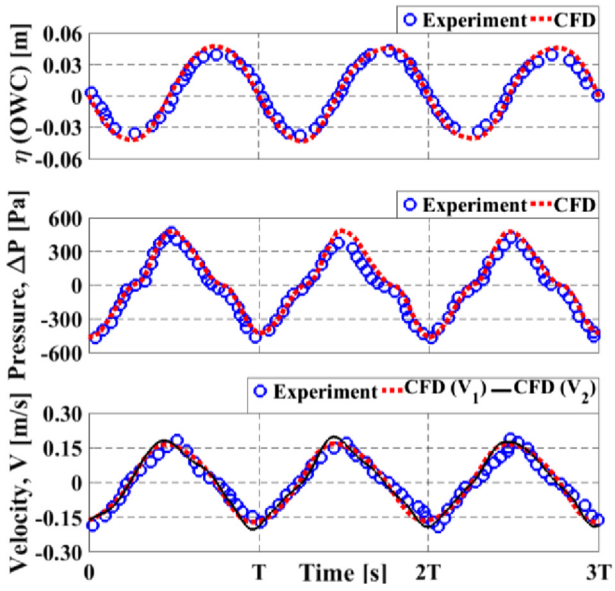

Fig. 4. Comparison between experiment (Kamath et al., 2015b) and CFD results for chamber free surface (water level) oscillation (η), chamber differential air pressure (ΔP) and chamber free surface velocity (V) under a wave condition of H = 120 mm and Kh = 1.26.

air mass flow rate by air density. However, experimentally it is usually defined as the product of the chamber's free surface velocity (rate of change of the wave level displacement, dη/dt) and the chamber's horizontal cross−sectional area (or the chamber's length in case of 2D model) assuming incompressible air. Although the first procedure for measuring the airflow rate is used in this paper, the free surface vertical velocity calculated from both procedures are compared against the experimental measurements. Fig. 4 compares the numerically measured time series data for free surface elevation inside the chamber (η) at chamber's centreline (b/2), differential air pressure (ΔP), free surface vertical velocity calculated from the air velocity measured through the PTO slot opening (1st procedure, V_1) together with applying the continuity equation and chamber's free surface vertical velocity (2nd procedure, V_2) calculated from its oscillation against the experimental data extracted from Kamath et al. (2015b). The experimental data uses a regular wave height of H = 120 mm and a wavelength that excites the device natural frequency presented by the dimensionless parameter Kh = 1.26, where K is defined as $K = \omega^2/g$. From this comparison, it can be noted that the experimental results have some uncertainties that can be clearly seen in variations between the subsequent peak and/or trough values, especially for the measured pressure and free surface oscillations, whereas CFD results seem to be more consistent/repeatable with standard deviations less than 2.5%. Qualitatively, the numerical model agrees well with the experimental data. Also, there is no significant difference between the two procedures used for measuring the air velocity (i.e., airflow rate), which is experimentally highlighted by Thiebaut et al. (2015) who found no significant differences in measuring the flow rate either by orifice pre−calibration and pressure measurement or by measuring the water column

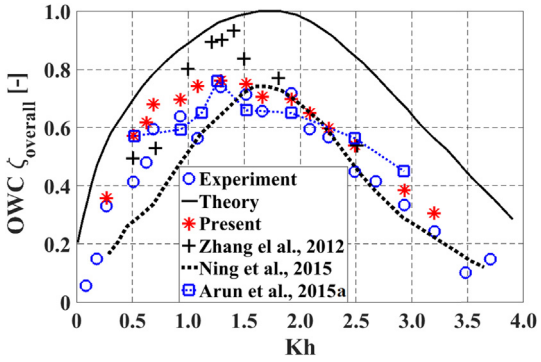

Fig. 5. OWC hydrodynamic efficiency comparison between experimental results (Morris-Thomas et al., 2007), analytical theory, others numerical models and present CFD results.

elevation inside the chamber. Additionally, the normalized root mean square deviation/error (López et al., 2014) of CFD results is within two standard deviations of the experimental data (calculated based on the available experimental time−series data).

In addition to validating the present model at the OWC natural frequency, simulating the device interactions with different wavelengths (steepness) are performed; the device overall hydrodynamic efficiency ($\zeta_{Overall}$) is illustrated in Fig. 5 in comparison with the analytical linear theory results (Evans and Porter, 1995), experimental measurements (Morris-Thomas et al., 2007) and others numerical results based on the Navier−Stokes equations (Ning et al., 2015; Zhang et al., 2012; Kamath et al., 2015a) over a range of Kh. Neglecting the wave nonlinearity as well as energy losses by viscous dissipation, the efficiency predicted by the linear wave theory represents the upper bound (extreme) with a peak value of $\zeta_{Overall\text{-}max}$ = 1.0 at the theoretical resonance frequency. On the other hand, the present CFD model agrees well with the experimental data even at the experimental resonance frequency (Kh = 1.26), where the experimental and CFD maximum efficiency is 0.74 and 0.76, respectively, which is less than 3% overestimation by CFD.

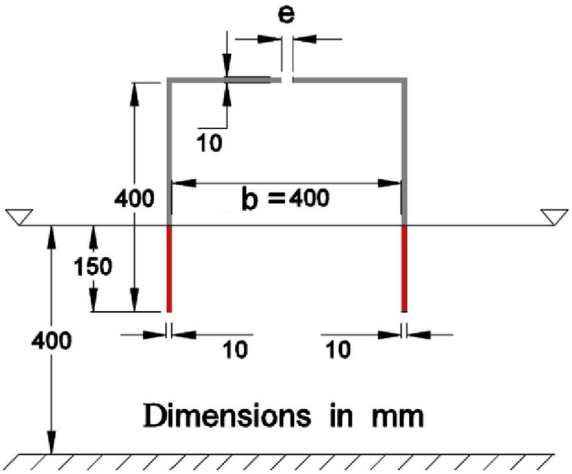

Fig. 6. Schematic of the stationary floating pile supported breakwater−OWC model tested by He and Huang (2014).

The second set of experiments used in the validation stage focuses on estimating the reflection (C_R), transmission (C_T), dissipation ($C_d = 1 - C_R^2 - C_T^2$) and pressure ($C_P = \Delta P / 0.5\rho g H$) coefficients resulting from regular waves interaction with a pile supported breakwater–OWC model (shown in Fig. 6) performed by He and Huang (2014). The validation uses a wave height of 35 mm over a range of wave periods represented by a non–dimensional ratio of the chamber length (b) to the incoming wavelength (L). The PTO damping is simulated by three slot opening ratios (defined as the slot opening size (e) divided by the chamber length) of 0.625%, 1.25% and zero (closed). The comparison of results illustrated in Fig. 7 shows that both the pressure and transmitted energy coefficients are captured well, whereas a little discrepancy found in the reflected energy coefficient, and as a result, the dissipation coefficient shows a slight deviation from the experimental data. These differences can be related to the methodology used in the experiment to resolve the incident and reflected waves, which is based on a two–point measurement procedure proposed by Goda and Suzuki (1976), while the present paper uses a three–point method proposed by Mansard and Funke (1980).

5. Stationary floating OWC model

The 1:50 floating–stationary OWC model shown in Fig. 8 is considered in the present study (with the same numerical wave tank dimensions and settings described in Section 2) to perform a series of numerical wave energy balance analysis. Considering the wave climate at the proposed deployment location of Bass Strait in southern Australia, a total of 102 numerical tests were performed under the following conditions at model scale: wave height, H = 50 mm and 100 mm, wave period (T) ranges from 0.8 s to 2.2 s with 0.1 s increment (corresponding to Kb = 1.8864–0.2494) and 11 slot opening (e = 1.5–9.0 mm) at a constant water depth, h = 1.5 m.

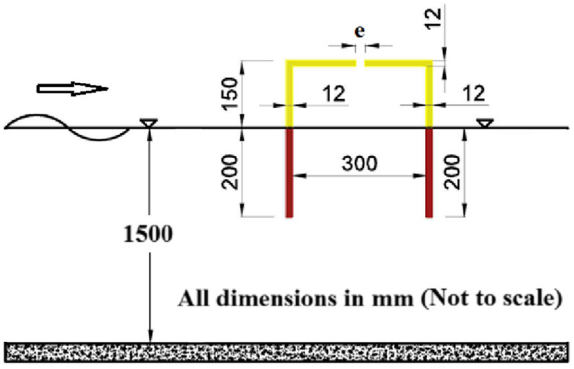

Fig. 8. Schematic of the 1:50 offshore stationary–floating OWC model considered in the present study.

6. Results and discussions

6.1. Overall OWC hydrodynamic performance

The device performance is initially investigated under a constant wave height of H = 50 mm for the whole Kb range with three different PTO damping values simulated by slot opening percentages (slot size/chamber length × 100) of 0.5, 1.0 and 2.0%, which are corresponding to a slot size (e) of 1.5, 3.0 and 6.0 mm, respectively. Generally, it is found that as the pneumatic damping increases, the pressure oscillation amplitudes (ΔP) increase (Fig. 9–a), while the airflow rate (q) (Fig. 9–b), as well as the chamber's free surface oscillation amplitude relative to the incident wave amplitude (amplification factor, η_{max}/A) (Fig. 9–c), decreases. This is in agreement with the experimental observations performed by Ning et al. (2016) for an onshore OWC. With the largest imposed damping (e = 1.5 mm or 0.5% opening slot), the pressure and the airflow rate have their maximum values of 117 Pa and 0.014 m^3/ms, accordingly when the device interacts with almost the lowest steepness (longest) waves

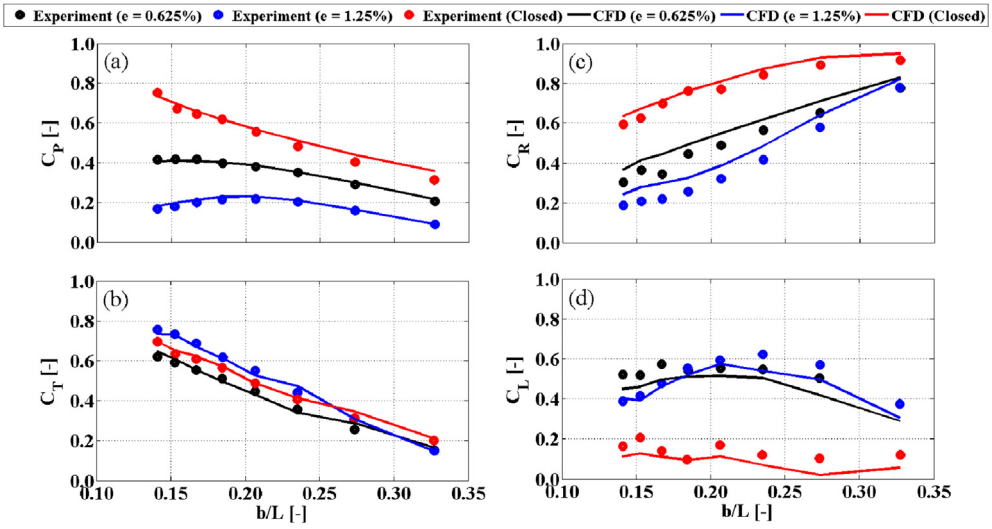

Fig. 7. Comparison between experimental (He and Huang, 2014) and CFD results for variations in (a): pressure coefficient (C_P), (b): transmission coefficient (C_T), (c): reflection coefficient (C_R) and (d): dissipation coefficient (C_d) versus b/L under a regular wave height of H = 35 mm.

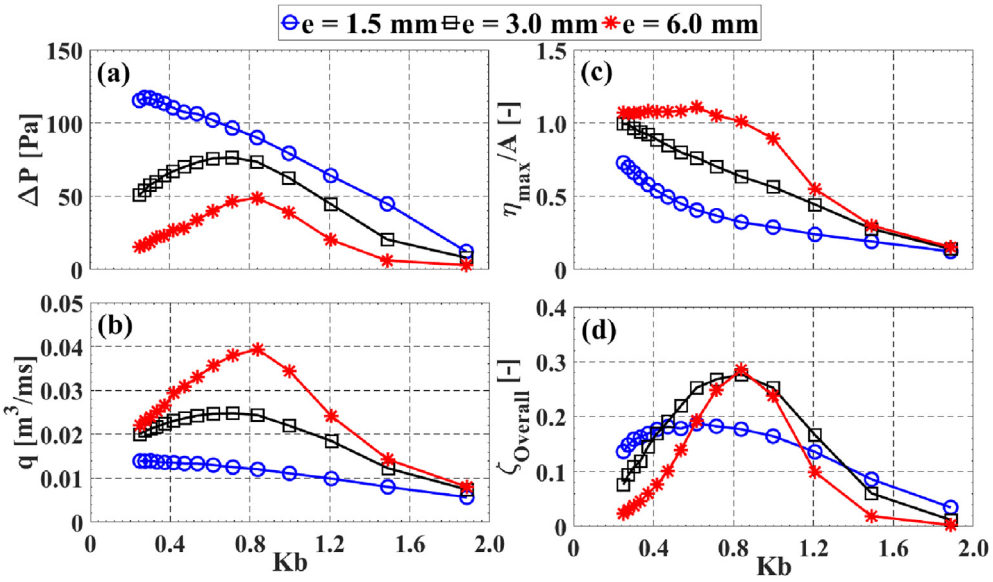

Fig. 9. Impact of the incoming wavelength on (a): chamber's differential air pressure (ΔP), (b): airflow rate (q), (c): chamber's free surface amplification factor (η_{max}/A) and (d): overall hydrodynamic efficiency ($\zeta_{Overall}$) over a range of Kb under three PTO damping values (e) and a wave height H = 50 mm.

(Kb = 0.2494–0.2738), which is the same pressure trend experimentally observed by He and Huang (2014) for a chamber with 0.625% slot opening; however, as Kb increases both quantities almost linearly reduce. It also worth mentioning that the corresponding pressure coefficient (C_P=ΔP/0.5ρgH) for ΔP = 117 Pa is 0.50, which is close to the value obtained by He and Huang (2014) and presented in Fig. 7 of the present paper, but this is smaller than a value of about 0.56 and 0.82 for onshore OWCs with 0.66% and 0.78% opening as presented in Ning et al. (2016) and Kamath et al. (2015b), respectively. This lower pressure coefficient can be assigned to the difference in hydrodynamic interactions with the offshore OWC that allows water waves to pass underneath the device, which in turn reduces the reflected waves and changes the wave envelope developed in front of device as will be discussed further in Section 6.2. On the other hand, both of the intermediate (e = 3.0 mm) and the lower (e = 6.0 mm) damping values result in nearly the same trends for the chamber differential air pressure and the airflow rate, which increase as the wavelength becomes shorter till peaked with ΔP = 76, 49 Pa and q = 0.025 and 0.039 m^3/ms at Kb = 0.616–0.714 and 0.8384 for the intermediate and the lower damping values, respectively, which is almost at the device natural frequency as reported in Iturrioz et al. (2015) for pressure measurements. This indicates that as the applied damping decreases the peak frequency of these parameters increases. After hitting these peaks, both variables diminish while Kb is advancing. The higher amplification factors (η_{max}/A) are observed to be 1.11, 1.0 and 0.73 for each damping value (lower–higher) when the device is subjected to the longest waves, and these values are gradually damped as the waves become shorter (i.e., higher steepness), except the case of the large damping (e = 6.0 mm) where a slight increase is observed till Kb = 0.616. For the device overall efficiency ($\zeta_{Overall}$) illustrated in Fig. 9–d, it is found that it initially increases with boosting the Kb until it tunes with maxima of 0.286, 0.277 and 0.187 at the device resonance frequency of Kb = 0.8384, 0.8384 and 0.616 associated with a damping of e = 6.0, 3.0, and 1.5 mm, accordingly, and then the efficiency declines with a further increase in Kb. Although the highest damping factor (e = 1.5 mm) results in a drop of about 0.11 in the maximum overall efficiency, it provides more frequency bandwidth allowing the device to be tuned to a wider wave frequency range. Also, the PTO damping of e = 3.0 mm provides almost the same maximum efficiency as e = 6.0 mm, but allows a broader frequency bandwidth.

Although Iturrioz et al. (2015) reported that the maximum pressure oscillation occurs close to the resonant period (except the case with a closed chamber), and in this case the maximum chamber free surface oscillations reach a maximum, Simonetti et al. (2015) and Ning et al. (2016) found that for a given OWC geometry, the maximum pressure amplitudes occur at higher frequencies than those for the chamber free surface oscillations. In the present study, results from Fig. 9 indicate that Iturrioz et al. (2015) findings are only valid for the case under the largest damping of e = 1.5 mm. Generally, the large pressure and airflow rate oscillations at a given pneumatic damping are not directly related to the chamber free surface oscillation, but rather its instantaneous slope is the important parameter. This importance can be described by considering that increasing the water vertical oscillation inside the chamber in a very short time (high frequency–short waves) results in a rapid change in the internal air pressure and forcing the air to evacuate the chamber through the PTO at high speed before air pressure equilibrium with the surrounding atmosphere occurs. In contrast, the slow change in the chamber's water oscillation associated with long waves, and even with large oscillation amplitudes, will displace a bigger amount of air out of the chamber but in a longer period.

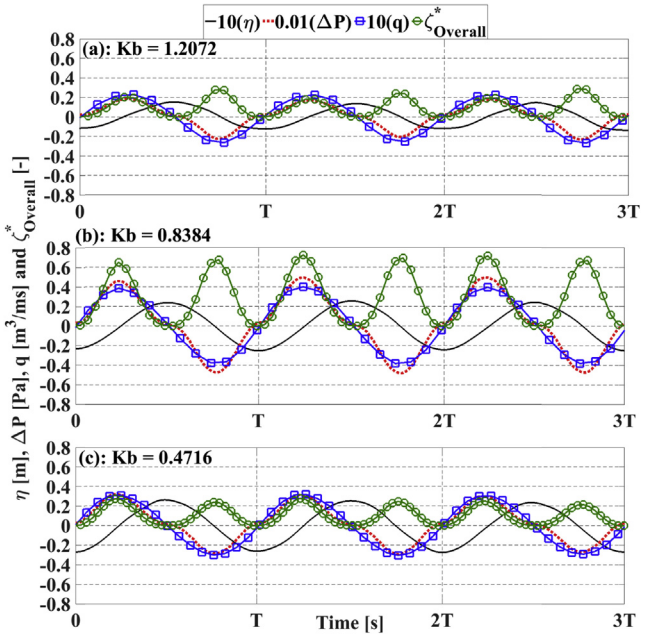

Fig. 10. Instantaneous chamber free surface oscillations (η), air pressure oscillations (ΔP), airflow rate (q) and overall hydrodynamic efficiency ($\zeta^*_{Overall}$) at different wavelengths (Kb) of 1.2072 (short), 0.8384 (intermediate) and 0.4716 (long) with a slot opening e = 6.0 mm and a wave height H = 50 mm.

In supporting the above explanation, Fig. 10 illustrates the instantaneous chamber free surface oscillation, differential air pressure, airflow rate and the overall efficiency (instantaneous overall efficiency, $\zeta^*_{Overall}$, which is defined as the ratio between instantaneous extracted pneumatic power = $\Delta P(t)\cdot q(t)$ and the incoming wave power P_I) for three wavelengths sorted as short (Kb = 1.2072), intermediate (Kb = 0.8384) and long (Kb = 0.4716) under a damping of e = 6.0 mm. It can be seen that the chamber free surface oscillation amplitudes at Kb = 0.4716 and 0.8384 are almost the same (η_{max}/A at Kb = 0.8384 is slightly lower than that at Kb = 0.4716 in Fig. 9–c); however, the shorter wave period with Kb = 0.8384 leads to a higher rate of change in the chamber free surface elevation (higher slope), which in turn produces higher pressure as well as airflow rate oscillation amplitudes. Conversely, for the shorter wave period of Kb = 1.2072, the oscillation amplitudes for both pressure and airflow rate are smaller than those for Kb = 0.8384, and this is due to the lower free surface oscillation inside the chamber with Kb = 1.2072, which causes the slow rate of change in the chamber internal water oscillation. It is also shown that as the wave frequency (Kb) increases, steepness (H/L) magnifies from 0.012 at Kb 0.4716 to 0.030 at Kb = 1.2072, and nonlinearity effects become more pronounced in the low pressure and airflow rate oscillations during the pressurizing stage. For these reasons, an asymmetric power extraction efficiency is observed clearly at Kb = 1.2072 with an inhalation (depressurizing) efficiency peak of almost 1.44 times that during the exhalation (pressurizing) stage.

Additionally, it worth noting that for the largest damping of e = 1.5 mm shown in Fig. 9, the maximum pressure oscillation, as well as the airflow rate, exists almost at Kb = 0.2494 together with the maximum free surface oscillation; however, the device overall efficiency is not at its maxima, which is achieved at a different Kb value of 0.616. According to Kamath et al. (2015a), this low efficiency with high chamber free surface oscillation and air pressure is related to the phase difference between both the pressure and the chamber's free surface vertical velocity (airflow rate). Actually, this phase difference is important to estimate the extracted power, but it cannot be considered as a direct indicator for the device efficiency; this is because the overall efficiency is defined as the ratio between the extracted and incident wave power. By this way, while the extracted power decreases with increasing pressure–airflow phase difference, the incident wave power increases with increasing the wave period (group velocity) (See Eqs. (8)–(11)). In addition, changing the wave period also affects every component in the energy conversion chain, which in turn alters the energy absorbed by the OWC (E_A) to extract from. For instance, time series of the chamber's free surface elevation, air pressure oscillation, airflow rate and the overall power extraction efficiency are presented in Fig. 11 at Kb = 0.2494 in comparison with results for Kb = 0.616. Despite the negligible phase difference between the power extraction parameters (pressure and airflow rate) for both Kb values, the overall efficiency is lower for Kb = 0.2494 than Kb = 0.616. For this reason, understanding the OWC performance in depth through the wave energy conversion chain is required.

6.2. OWC energy conversion chain

The different parameters describing the energy conversion chain (demonstrated in Fig. 2 and summarised in Table 1) are shown in Fig. 12 where it can be seen that the device tends to reflect most of the incoming wave energy as the wavelength becomes shorter (Fig. 12–a). Also, the reflection coefficient (C_R) increases with increasing pneumatic damping, but this effect becomes nil for the shorter waves with Kb almost greater than 1.5. On the other side, the transmitted energy

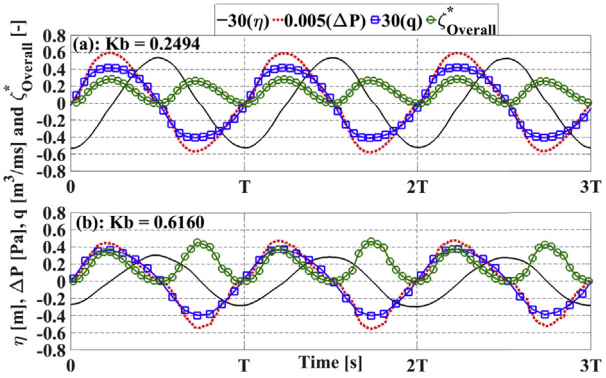

Fig. 11. Instantaneous chamber free surface oscillations (η), air pressure oscillations (ΔP), airflow rate (q) and overall hydrodynamic efficiency ($\zeta^*_{Overall}$) at different wavelengths (Kb) of 0.2494 and 0.616 with a slot opening (e) = 1.5 mm and a wave height H = 50 mm.

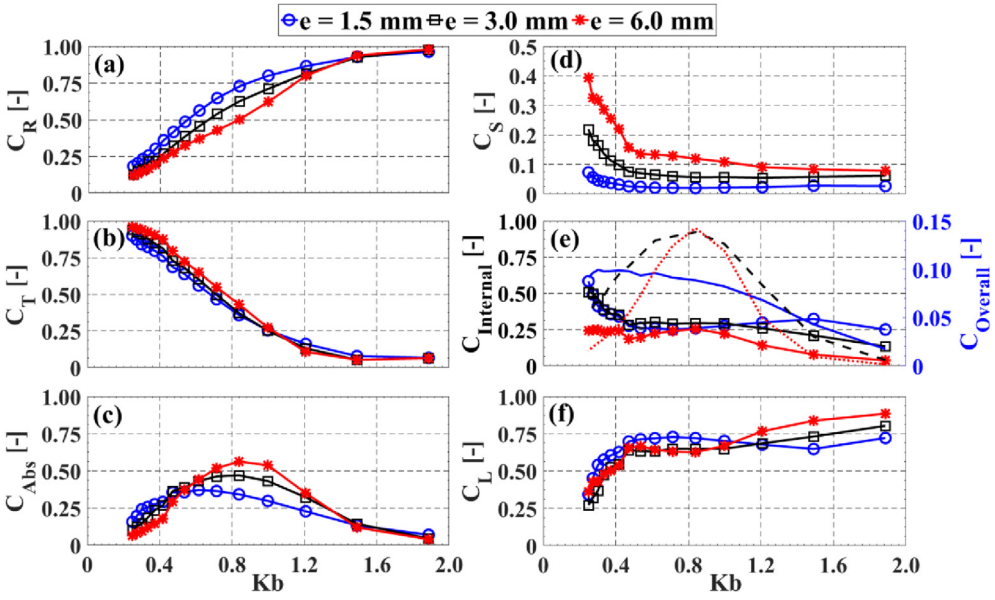

Fig. 12. OWC energy balance coefficients for three PTO damping values over a range of Kb and a wave height H = 50 mm including (a): reflection (C_R), (b): transmission (C_T), (c): energy absorption (C_{Abs}), (d): energy stored (C_S), (e): internal and overall energy extraction ($C_{Internal}$ and $C_{Overall}$) and (f): energy losses (C_L). Solid, dashed and dotted lines in subplot (e) correspond to a slot opening of e = 1.5, 3.0 and 6.0 mm, respectively for $C_{Overall}$.

represented by the transmission coefficient (C_T) in Fig. 12–b has completely an opposite trend to the reflection coefficient. Consequently, for longer waves, most of the incident energy passes underneath the OWC chamber. In addition, the higher PTO damping results in a slight reduction in the transmission coefficient, yet this effect occurs a little after Kb = 1.0. Considering the variation in the reflection and transmission coefficients, it is expected that the maximum energy absorption coefficient (C_{Abs}) is located in a bandwidth away from the Kb extremes as shown in Fig. 12–c. It is also shown that the device has a maximum energy absorption coefficient of 0.56, 0.47 and 0.37 almost at the device resonance of Kb = 0.8384, 0.8384 and 0.616 corresponding to a PTO damping of e = 6.0, 3.0 and 1.5 mm, respectively.

Having the amplification factor trends illustrated in Fig. 9–c, the OWC model seems to have a tendency to store more energy in the chamber's free surface heave motion under longer waves and smaller PTO damping as shown in Fig. 12–d. Furthermore, as Kb develops, the amplification factor lessens, and the energy absorption coefficient increases till peaked, which in turn results in progressively decreasing the energy storage coefficient almost up to Kb = 0.8384. Afterwards, the energy storage coefficient becomes nearly steady as a result of decreasing the absorped energy coefficient, while the amplification factor remains falling.

Regarding the overall energy extraction capability of the device, it can be seen in Fig. 12–e (right axis) that the OWC tends to extract most of the incoming wave energy at the intermediate frequency range with a maximum overall extraction coefficient ($C_{Overall}$) of 0.143 at Kb = 0.8384, 0.138 at Kb = 0.8384 and 0.099 at Kb = 0.3018–0.4716 for slot opening e = 6.0, 3.0 and 1.5 mm, respectively. Similar to the overall efficiency (Fig. 9–d), the intermediate damping of e = 3.0 mm provides more frequency bandwidth. On the other hand, the system ability to extract apart of absorbed energy, which is defined by the internal energy extraction coefficient ($C_{Internal}$) shown in Fig. 12–e (left axis). It is obvious that $C_{Internal}$ has a contrary trend to the energy losses coefficient in Fig. 12–f, but both have almost a steady trend over the intermediate frequencies where $C_{Overall}$ is high. Before discussing the energy losses in the OWC system in more detail, it is worth noting that the possible sources include hydrodynamic losses, which represent the underwater part up to the free surface interface as well as the aerodynamic losses resulting mainly from the airflow into and out of the chamber through the PTO. The hydrodynamic losses involve the friction head losses coming from the chamber free surface interaction with the OWC non–slip walls. These losses heavily depend upon the water amplification (i.e. contact length with OWC walls), free surface vertical velocity and friction coefficient, which is related to the Reynolds number together with the walls roughness. In addition to the friction/viscous losses, the chamber sharp lips enforce the water particles to change their travelling direction, and then accelerate the flow at those regions inducing flow separation and vortex formation. This kind of loss is wave frequency dependent due to its coupling with the water particles orbital motion, which changes under different frequency, and consequently, its interaction with the chamber lips of a given thickness will be different.

As discussed in Section 6.1, throughout the whole tested frequency (Kb) range, the airflow rate (Fig. 9–b), as well as the amplification factor (Fig. 9–c), is inversely proportional to the applied pneumatic damping. This indicates that the viscous losses also follow the same trend. Under the longest wave (Kb = 0.2494), the incoming wave energy is maximum (Eq. (2)), but the energy absorption coefficient (C_{Abs}) is low and diminishes with reducing the PTO damping. Considering the extracted energy' parameters (airflow rate and pressure

amplitudes) in Fig. 9, the device tends to extract most of the absorbed energy (i.e., maximum $C_{Internal}$) at this frequency. However, in comparison with the incoming wave energy, the overall energy extraction coefficient ($C_{Overall}$) is minima at this frequency for damping e = 3.0 and 6.0, which can be assigned to the large difference between this frequency (Kb = 0.2494) and that where both airflow rate and pressure amplitudes are peaked for these damping. This maximum $C_{Internal}$ together with the energy conservation principle in Eq. (7) result in minimum losses coefficients (C_L). Furthermore, as the water particles have longer orbital motion under longer wavelength, which leads to longer particle excursion and lesser vortex formations at the chambers' lips (further flow field results are discussed in Section 6.5). These characteristics contribute to the smaller losses coefficient for the different damping values shown in Fig. 12–f under longer waves.

With a further increase in Kb, the wave steepness magnifies, and nonlinearity arises together with the water particles excursions become shorter leading to stronger vortex generation and breaking the chamber flat (piston–rigid) internal free surface motion. These effects result in increasing the losses coefficient, and eliminate magnifying the extracted energy' parameters significantly, especially for the intermediate and high damping, whereas the energy absorption coefficient increases. Consequently, the internal energy extraction coefficient reduces, except under the lower damping (e = 6.0 mm) that shows a steady trend indicating reasonable improvements in the air pressure and airflow rate as the absorbed energy increases. Moreover, the energy chain in Fig. 2 demonstrates the direct coupling between the stored energy and other possible sinks, which further explains the changes in the internal energy extraction and losses coefficients. For instance, as Kb increases, the energy stored coefficient decreases, and the amount of this decreased energy seems to escalate the energy losses more than be converted to pneumatic energy for damping e = 1.5 and 3.0 mm, but this is not the case for the lower damping of e = 6.0 mm. During the intermediate frequency bandwidth (Kb = 0.4716–0.9978), the changes in the energy stored, energy losses and internal energy extraction coefficients are negligible, while the absorbed energy coefficient increases and the incoming wave energy decreases, which in turn results in the maximum overall energy extraction coefficient almost at the same frequency of the maximum energy absorption coefficient. Out of this frequency range, it is expected that the losses show more reduction as a result of the reduction in the airflow rate and chamber's free surface amplification; however, the losses coefficients show higher values at the maximum tested frequency of Kb = 1.8864. This can be assigned to the further shortening in the wavelength, nonlinearities escalation, the lower energy extraction and absorption coefficients and the steadiness of the stored energy coefficient.

6.3. PTO damping and wave height effects on OWC overall performance

In order to discover the impact of the PTO damping together with the incident wave height on the offshore OWC model performance in more detail, a series of two–dimensional damping factors (C = b/e) defined as the ratio between the chamber length (b) and the slot opening size (e) are studied. Eleven different slot opening sizes (e = 1.5, 2.0, 2.5, 3.0, 3.5, 4.0, 5.0, 6.0, 7.0, 8.0 and 9.0 mm) are applied for three different incident wavelengths corresponding to Kb = 0.4716, 0.8384 and 1.2072 under two wave heights of H = 50 mm and 100 mm.

Starting with the PTO impact, the chamber differential air pressure amplitude (ΔP), the airflow rate amplitude through the PTO (q), the chamber free surface amplification factor (η_{max}/A) and the overall hydrodynamic efficiency ($\zeta_{Overall}$) for the different PTO damping values and wavelengths under a regular wave height of 50 mm are presented in Fig. 13. The chamber differential air pressure is seen to gradually increase with growing the damping factor (C) from 33.33 (e = 9.0 mm) to 200 (e = 1.5 mm) as shown in Fig. 13–a. On the contrary, airflow rate and chamber free surface amplification factor decrease as the pneumatic damping accumulates as illustrated in Fig. 13 b and c, accordingly. Throughout the entire simulated damping factors, always the shorter wavelength (Kb = 1.2072) results in the minimum pressure, airflow rate and amplification factor, whereas the intermediate wavelength (Kb = 0.8384) produces the largest chamber air pressure and airflow rate amplitudes up to a damping factor C = 100 before the longer wavelength (Kb = 0.4716) starts taking place instead. A maximum pressure of 108 Pa is observed at the largest damping of C = 200 with the longer wavelength, while the airflow rate peaks at 0.046 m^3/ms with the intermediate wavelength under the lowest PTO damping of C = 33.33.

Overall, it can be seen that for the entire PTO damping range investigated, the chamber's amplification factor declines with decreasing incoming wavelength. The observed maximum chamber free surface oscillation amplitudes (η_{max}) are about 1.21, 1.14 and 0.61 times the incident wave amplitude under the lowest applied damping for the three simulated wavelengths corresponding to Kb = 0.8384, 0.4716 and 1.2072, accordingly; however, these oscillations are progressively damped to about 0.32, 0.50 and 0.24, respectively as the PTO damping boosts to its maximum (C = 200).

In Fig. 13–d, the device overall efficiency continues rising with increasing PTO damping, then reaches peak values at a specific damping factor over a narrow damping range before declining. Considering the longer wavelength (Kb = 0.4716), the overall efficiency increases from 0.058 at a damping factor of C = 33.33 to about 0.2 at C = 120, and then slightly drops by 0.021 under the maximum damping of C = 200. For the simulated shorter wavelength (Kb = 1.2072), a similar trend as the longer wavelength is observed; however, the maximum efficiency is found to be 0.035 less at the same damping factor of C = 120. On the other side, with the intermediate wavelength (Kb = 0.8384), the maximum efficiency occurs at a low damping factor of C = 60–75, and it is found to be approximately 0.3; however, with either decreasing or increasing the applied damping out of the optimum value, the efficiency moves down to about 0.23 and 0.18 for the minimum and maximum exerted damping factors, respectively. These

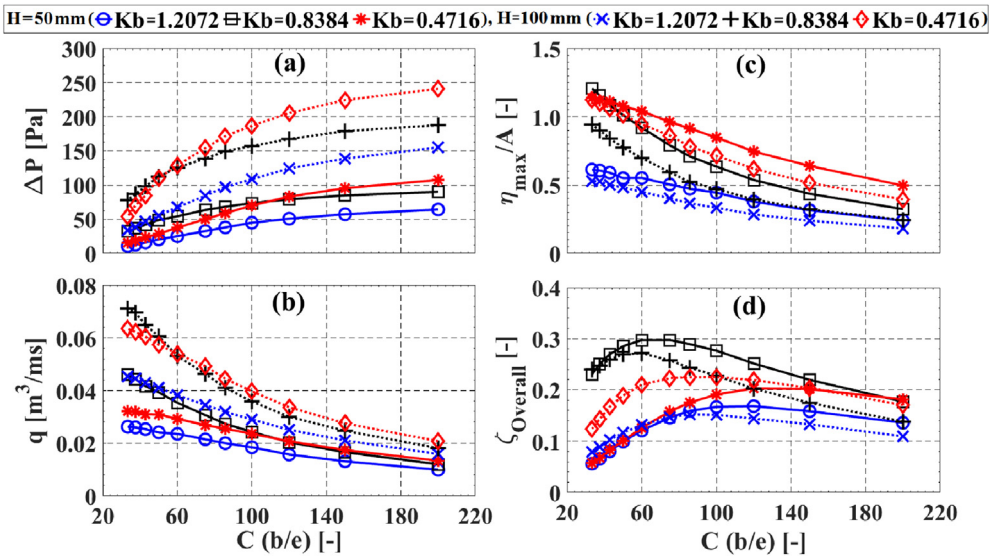

Fig. 13. Impact of PTO damping factor (C) on (a): variation in chamber differential air pressure (ΔP), (b): airflow rate (q), (c): chamber free surface amplification (η_{max}/A) and (d): the overall hydrodynamic efficiency ($\zeta_{Overall}$) under two wave heights H = 50 and 100 mm.

variations highlight the possibility of extracting power out of the designed resonance frequency by altering the PTO damping in order to tune the device to the incoming wavelength. In comparison with onshore OWCs, numerical CFD results from Kamath et al. (2015b) show the same general trends of all measured variables presented in Fig. 13. However, the measured values are larger for onshore OWCs. For instance, considering a wave height of 50 mm, the maximum overall efficiency for the offshore OWC is found to be 0.3 for the intermediate wavelength, where a value of about 0.83 was reported by Kamath et al. (2015b) for a 60 mm wave height under an intermediate wavelength. Again, this may be a consequence of the measured smaller pressure and airflow rate for the offshore OWC.

Although increasing the PTO damping factor (C) leads to increasing air pressure, the chamber free surface oscillation decreases. Consequently, the airflow rate drops down at a given frequency. This can be explained by studying the impact of three PTO damping corresponding to a slot opening e = 9.0, 5.0 and 1.5 mm on the instantaneous chamber free surface elevation, air pressure, airflow rate and the overall hydrodynamic efficiency at a given wavelength of Kb = 0.8384 as shown in Fig. 14. Considering that the chamber free surface vertical velocity is defined as the rate of change in its oscillation ($d\eta/dt$), which simply can be presented by $(\eta_{crest}-\eta_{trough})/T$, it is found that the free surface oscillation decays with enlarging the applied damping while the wave period (T) (wavelength) is fixed; accordingly, this slows down the free surface oscillation rate, and as a consequence, the airflow rate also deteriorates.

In addition, Fig. 14 illustrates that increasing the pneumatic damping also has an impact on the power extraction parameters (pressure and airflow rate) through the whole operation cycle. By escalating the damping from e = 9.0 mm to 1.5 mm, the air pressure and airflow rate change from having higher magnitudes during the pressurizing stage to larger values during the air suction process, respectively. As a consequence, the OWC device tends to extract the incoming wave power with a maximum overall instantaneous efficiency during the exhalation of about 1.16 times that during inhalation stage under a low damping of e = 9.0, while this value drops to 0.81 at e = 1.5 mm.

The relevance of increasing the incoming wave energy to the device performance is investigated by doubling the incident wave height to 100 mm, which escalates the incoming wave energy four times (Eq. (2)). Generally, it can be seen that

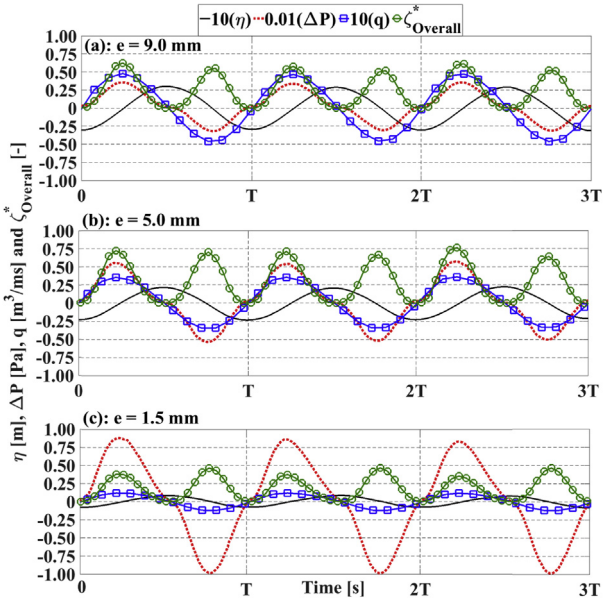

Fig. 14. Instantaneous chamber free surface oscillations (η), air pressure oscillations (ΔP), airflow rate (q) and overall hydrodynamic efficiency ($\zeta^*_{Overall}$) under different PTO of a slot opening e = 9.0, 5.0 and 1.5 mm for a wavelength of Kb = 0.8384 and height H = 50 mm.

the overall trend of the air pressure, airflow rate, amplification factor and the overall efficiency presented in Fig. 13 are similar to those with the lower wave height. The air pressure oscillation amplitudes in Fig. 13–a seems to increase as the wave height increases, and this effect gradually decreases as the damping factor increases with a maximum amplitude of about 3.47, 2.44 and 3.18 times values with the smaller wave height (H = 50 mm) corresponding to a wavelength of Kb = 0.4716, 0.8384 and 1.2072, respectively at C = 33.33 in comparison with almost 2.24, 2.08 and 2.42 at C = 200. Similar to the impact of increasing the wave height on the pressure amplitudes, the airflow rate amplitudes also increase to about 1.5–2.0 times the corresponding values with the 50 mm wave height at the lowest damping, and this impact slowly weakens to 1.5–1.6 as the damping increases to its maximum. In contrast, the amplification factors are inversely proportional to the wave height over the entire tested damping factors. The discrepancy between the impact that the wave height has on reducing the amplification factor and increasing the airflow rate for a given Kb value can also be assigned to the fact that the amplification factor represents the chamber's free surface oscillation amplitude relative to the incident wave amplitude, which increased two times. As a result, decreasing the amplification factor does not mean decreasing the absolute oscillation amplitude (unless for a constant wave height). Also, considering that the airflow rate is coupled with the chamber's free surface slope not its oscillation amplitude, which again is illustrated in Fig. 15–b for a wavelength of Kb = 0.8384, a damping of e = 6.0 mm and wave heights of 50 and 100 mm. Results clarify that although increasing the wave height to 100 mm resulted in a lower amplification factor, the chamber free surface oscillation amplitude is larger than that with 50 mm wave height of the same frequency (Kb = 0.8384); therefore, the free surface slope (with respect to the time axis) is larger with the higher wave, which in turn produces higher free surface velocity and airflow rate.

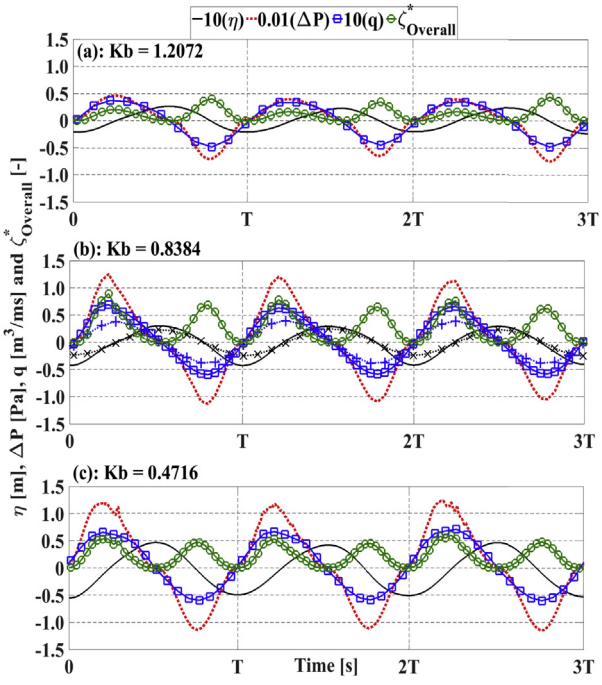

Fig. 15. Instantaneous chamber free surface oscillations (η), air pressure oscillations (ΔP), airflow rate (q) and overall hydrodynamic efficiency ($\zeta^*_{Overall}$) at different wavelengths of Kb 1.2072, 0.8384 and 0.4716 for a wave height H = 100 mm with a slot opening e = 6.0 mm. The dotted line with x markers in subplot (b) refers to η at H = 50 mm.

For the overall hydrodynamic efficiency shown in Fig. 13–d, increasing the incident wave height results in decreasing the device maximum efficiency at Kb = 0.8384 by about 0.025, shifting the optimum damping to lower values and narrowing its range. The reduction in the efficiency is more pronounced under high PTO damping. In contrast, under small and intermediate damping factors, there a little increase in the efficiency for the shorter waves (Kb = 1.2072), and this improvement is more noticeable for the longer wavelength (Kb = 0.4716) where the overall efficiency increases with increasing wave height with a peak efficiency at a damping of C = 75–120 approximately 0.022 higher than that under 50 mm wave height at damping C = 120, which indicates that for higher waves (energetic seas), the offshore OWCs can extract more energy over a wider frequency bandwidth.

In comparison with the results of the smaller wave height (H = 50 mm) shown in Fig. 10, the larger incoming wave height (H = 100 mm) introduces more nonlinear effects throughout the whole frequency range as demonstrated in Fig. 15 for three wavelengths. Moving from longer waves (Kb = 0.4716) with steepness of 0.024 to shorter waves (Kb = 1.2072) with 0.06 steepness, results in changing the air pressure and airflow rate crests and troughs from having higher crests to deeper troughs at steeper waves. Consequently, the OWC overall instantaneous efficiency peak changes from being larger during exhalation with about 1.28 times the inhalation efficiency at Kb = 0.4716 to only 0.45 at Kb = 1.2072, which is smaller than that of 0.7 achieved with a 50 mm wave height at the same frequency (Kb = 1.2072).

6.4. Impact of PTO damping and wave height on OWC energy balance

The results of varying the PTO damping and increasing the wave steepness (wave height) on each component involved in the wave–pneumatic energy conversion process are presented in Fig. 16. Fig. 16–a shows that the reflection coefficient (C_R) increases as the applied damping, as well as the wave height, increases. In addition, over all damping factors investigated, the reflection coefficient increases as the wavelength becomes shorter. On the other side, the transmitted energy coefficient (C_T) in Fig. 16–b shows a contrary trend to the reflection coefficient. Thus, the OWC transmission coefficient tends to slightly decrease with increasing the PTO damping and wave height. An exception found for the shorter wavelength (Kb = 1.2072), which shows a slight increase with increasing the damping and insignificant response to the wave height. For damping factors larger than C = 120, the transmission coefficient becomes insensitive to the applied damping.

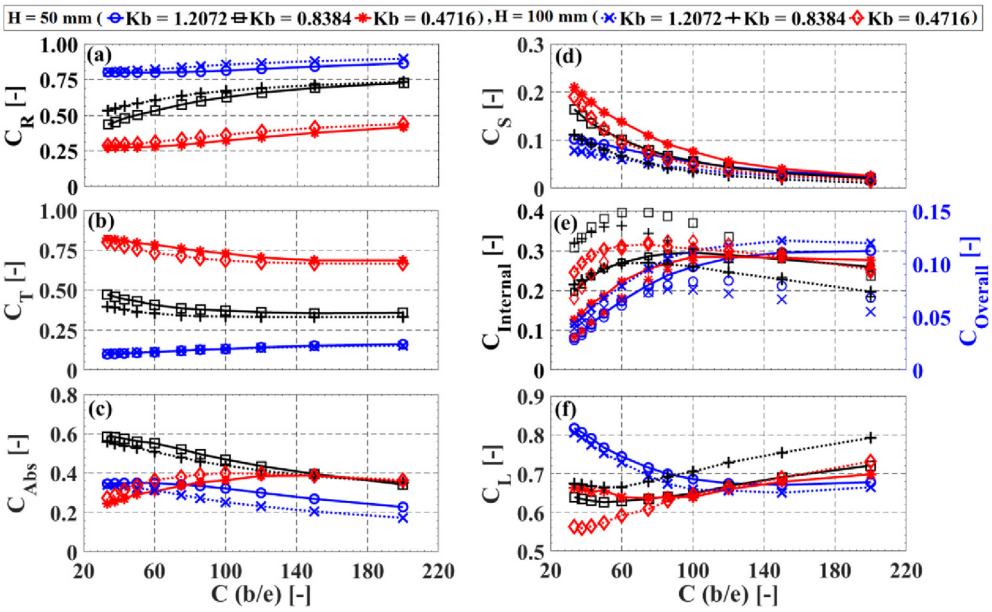

Fig. 16. OWC energy balance coefficients vs. PTO damping factor (C) under two wave heights H = 50 and 100 mm including (a): reflection (C_R), (b): transmission (C_T), (c): energy absorption (C_{Abs}), (d): energy stored (C_S), (e): internal and overall energy extraction ($C_{Internal}$ and $C_{Overall}$) and (f): energy losses (C_L). Markers without lines in subplot (e) refer to $C_{Overall}$.

For the energy absorption coefficient (C_{Abs}) in Fig. 16–c, under the shorter (Kb = 1.2072) and intermediate (Kb = 0.8384) wavelengths, this coefficient falls down with a further increase in the PTO damping as well as the incident wave height. Overall, the shorter wavelength (Kb = 1.2072) provides almost the lowest absorption coefficient, while the device tends to absorb more energy more efficiently as the damping and wave height increase when being subjected to the longer wavelength (Kb = 0.4716).

Similar to the observed impact of increasing the pneumatic damping and the wave height on the amplification factor (Fig. 13–c), the energy stored coefficient shown in Fig. 16–d also follows the same trend of the amplification factor. Regarding the device internal energy extraction coefficient ($C_{Internal}$) illustrated in Fig. 16–e, it seems that as the damping increases, $C_{Internal}$ arising till a certain damping that represents the optimum value for a given wavelength, and then it tends to slightly decrease with further increasing the applied damping. Furthermore, as the wave height increases, the device's $C_{Internal}$ increases except the intermediate wavelength (Kb = 0.8384) that shows a reduction in the internal energy extraction coefficient after a damping factor C = 60. Similar impacts of the applied damping on the overall energy extraction coefficient are observed (Fig. 16–e), but increasing the wave height only improves the overall energy extraction coefficient under the longer wavelength (Kb = 0.4716) as found for the overall efficiency in Fig. 13–d.

In addition to having an opposite trend to the internal energy extraction coefficient, the losses coefficient in Fig. 16–f gradually decreases as the damping increases until achieving a minimum value at almost the same damping corresponds to maximum $C_{Internal}$. Following this minima, the losses coefficient begins to move up following the increase in the PTO damping. Also, the shorter wavelength (Kb = 1.2072) shows lesser sensitivity to the higher damping factors. Except the intermediate wavelength, which produces higher losses coefficient with increasing the wave height especially after the optimum damping of C = 60, increasing the wave height results in further reductions of the losses coefficients for Kb = 1.2072 over all damping and for Kb = 0.4716 when the damping factor (C) is less than 100. It is, however, important to note that this drop in the losses coefficient is a representation for the energy losses relative to the absorbed energy, and this does not mean that the absolute energy losses are reducing with increasing the wave height. As one can expect, increasing the wave height raises the nonlinear effects, which can result in increasing the energy losses. Evidence for supporting and clarifying this argument is given in Fig. 17 for the absolute energy values corresponding to every component in the energy balance model under a wavelength of Kb = 0.4716 and a pneumatic damping of e = 5.0 mm (C = 60) for both wave heights of H = 50 mm and 100 mm. Results show that under the higher wave (H = 100 mm), each energy component in the energy balance model is larger than that for H = 50 mm. Also, the energy losses in the system when being subjected to the 100 mm wave height is about 4.4 times that with 50 mm wave height. More details about the vortex formation in the OWC is discussed in the following section.

6.5. Flow visualization and vortex generation

Flow visualization provides more information about the flow field, which highlights the areas of interest where energy can be dissipated and/or stored such as locations of stronger vortices and chamber free surface sloshing, respectively. The capability of the numerical model used herein for capturing

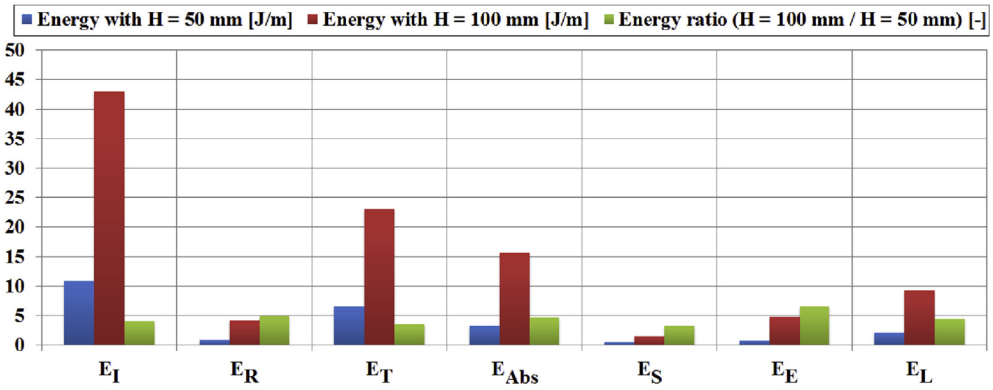

Fig. 17. OWC energy balance comparison between two wave heights of 100 mm and 50 mm at a wavelength of Kb = 0.4716 and a damping factor of C = 60 (e = 5.0 mm).

the flow behaviour, vortex generation and dissipation has previously been validated by the authors (Elhanafi et al., 2016b) against PIV data from model scale experiments for a fixed–bottom standing OWC. In this section, the same settings/meshing required at the virtual field of view implemented by Elhanafi et al. (2016b) are applied on the current model to discover the influence of different design parameters such as the incoming wave frequency, wave height and PTO damping on the flow behaviour inside the considered fixed offshore OWC (Fig. 8). The flow field is discovered

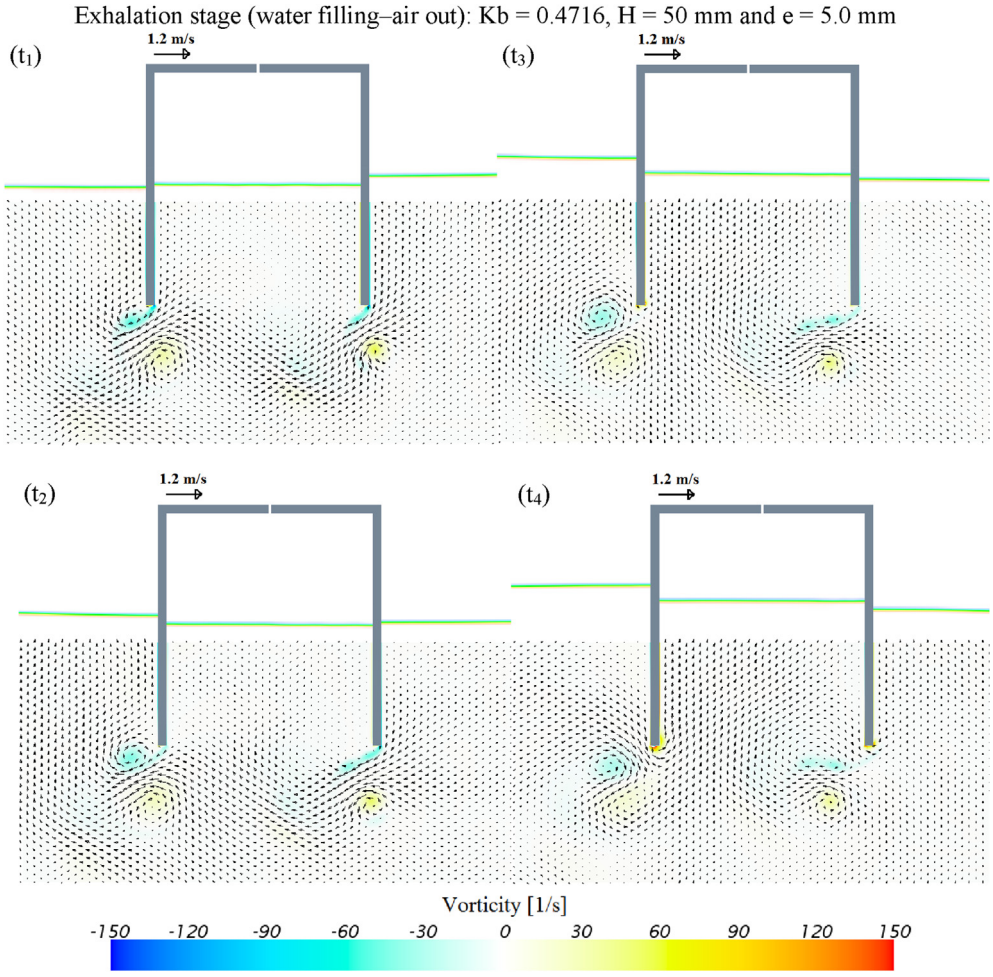

Fig. 18. Flow field during the exhalation stage for a constant 50 mm wave height and a damping of e = 5.0 mm slot opening under a wavelength of Kb = 0.4716. (Wave propagation direction →).

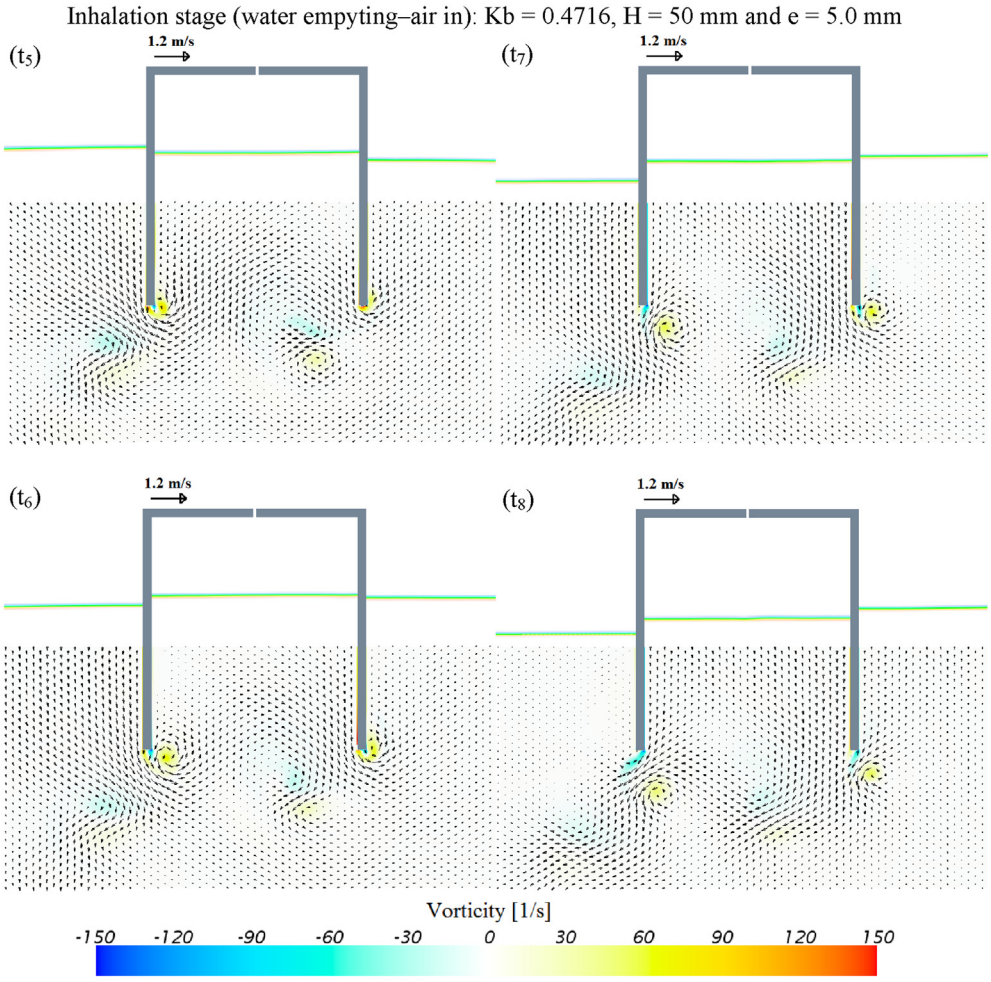

Fig. 19. Flow field during the inhalation stage for a constant 50 mm wave height and a damping of e = 5.0 mm slot opening under a wavelength of Kb = 0.4716.

through eight phases (t_1 – t_8) representing one wave cycle with a T/8 time increment between each phase. The first phase (t_1) starts when the chamber free surface level is minimum (trough).

Figs. 18 and 19 visualize the water flow through the OWC model during the exhalation (inflow—water filling the chamber or pressurizing—pushing air out of the chamber) and inhalation (outflow—water falling/emptying the chamber or depressurizing—air sucking into the chamber) stages, accordingly for a fixed PTO damping represented by e = 5.0 mm, a constant wave height of 50 mm and under a wavelength of Kb = 0.4716. Starting when the water level inside the OWC chamber is at its minima (t_1), the velocity magnitudes inside the chamber are still quite small. In addition, the vortices generated from the passed emptying process are clearly visible and extend towards the incoming ocean waves. These vortices consist of clockwise vortices (negative) positioned underneath the chamber lips, while anti—clockwise vortices (positive) are located under the negative vortices at both of the front and rear lips. Furthermore, as the water level moves upward, the velocity field increases and vortices start to strengthen till the maximum inflow occurs when the chamber free surface restores its initial still water level (mean zero level at t_3). At this instant, the generated clockwise vortices start detaching from the chamber lips, and small counter—clockwise vortices following the wave propagation direction begin taking place just below the submerged walls, which become obvious at t_4. Following this phase, the clockwise vortices begin to dissipate and move towards the seabed, whereas the wall—attached positive vortices initially observed at t_3 keep escalating and travelling upward with higher strength being assigned to the vortices at the ocean side wall. This process continues developing until the exhalation process ends, and the inhalation stage initiates at t_5 when the chamber free surface reaches its peak. When the inhalation stage commences, the velocity field begins to re—increase towards a maximum at the outflow instant (t_7). During this process, the anti—clockwise vortices keep building up with a reversed travelling direction (i.e., following the water level falling direction). In addition to these vortices, clockwise vortices attached to the walls' tips appear while the anti—clockwise vortices begin to separate from the lips. With further downward chamber water level movement towards the end of the emptying stage, the anti—clockwise vortices become weaker, whereas the clockwise vortices grow up till retaining the same characteristics as at t_1.

In order to uncover the impact of the incoming wavelength on the flow field, instantaneous shots are illustrated in Fig. 20 for additional three different Kb values of 0.2494, 0.8384 and

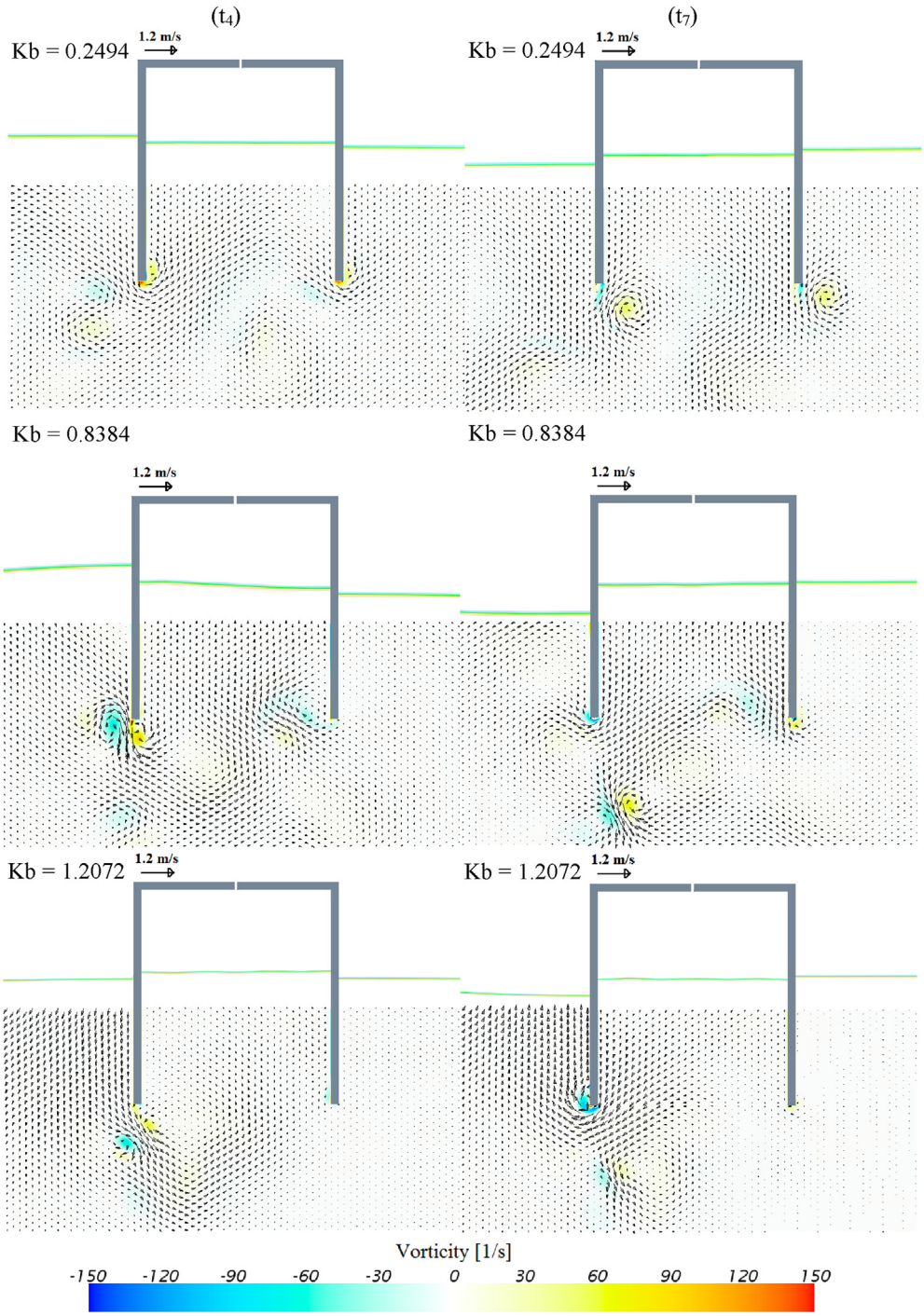

Fig. 20. Wavelength impact on the flow field for a constant 50 mm wave height and a damping of 5.0 mm slot opening.

1.2072. Generally, it is found that as the wavelength decreases, the vortex generation and dissipation processes significantly change. The magnitude and size of the clockwise vortices increase compared with the longest waves (Kb = 0.2494) especially for the resonance wavelength (Kb = 0.8384) during the exhalation stage (t_4). The negative vortices associated with the shorter waves (Kb = 1.2072) are almost of the same magnitudes as those at the resonance wavelength; however, their sizes are smaller and larger during the inflow and outflow, accordingly. In addition, as the waves become shorter, most of the generated vortices at chamber's front lip are located out of the chamber (i.e. no longer behind the front wall). This can be due to the increase in the free surface oscillation frequency associated with the incoming wave frequency, which does not provide enough time for the water particles to completely change their direction towards the chamber's top side.

Furthermore, during the outflow stage, the dominate vortices at the sea wall change from being anti–clockwise to

clockwise as the wavelength shortens. Also, the vortex generation at the lee side diminishes as the wavelength decreases (high steepness), and becomes almost invisible for the shorter wavelength (Kb = 1.2072), which can be attributed to the associated reduction in the energy transmission coefficient with reducing the incoming wavelength (see Fig. 12–b). In addition, increasing the wave steepness by decreasing the wavelength, raising the nonlinearity, which obviously affects the chamber free surface flatness. Accordingly, with the longest wave, the free surface seems to move as a rigid piston, while sloshing and free surface distortion increase as the wavelength decreases.

For the PTO damping effects, Fig. 21 shows the impact of changing the applied PTO damping of e = 1.5, 5.0 and 9.0 mm on the flow behaviour under 50 mm wave height and a constant wavelength of Kb = 0.8384. It is found that during the inflow stage, the clockwise vortices generated around the front wall are almost of the same magnitudes with slightly larger

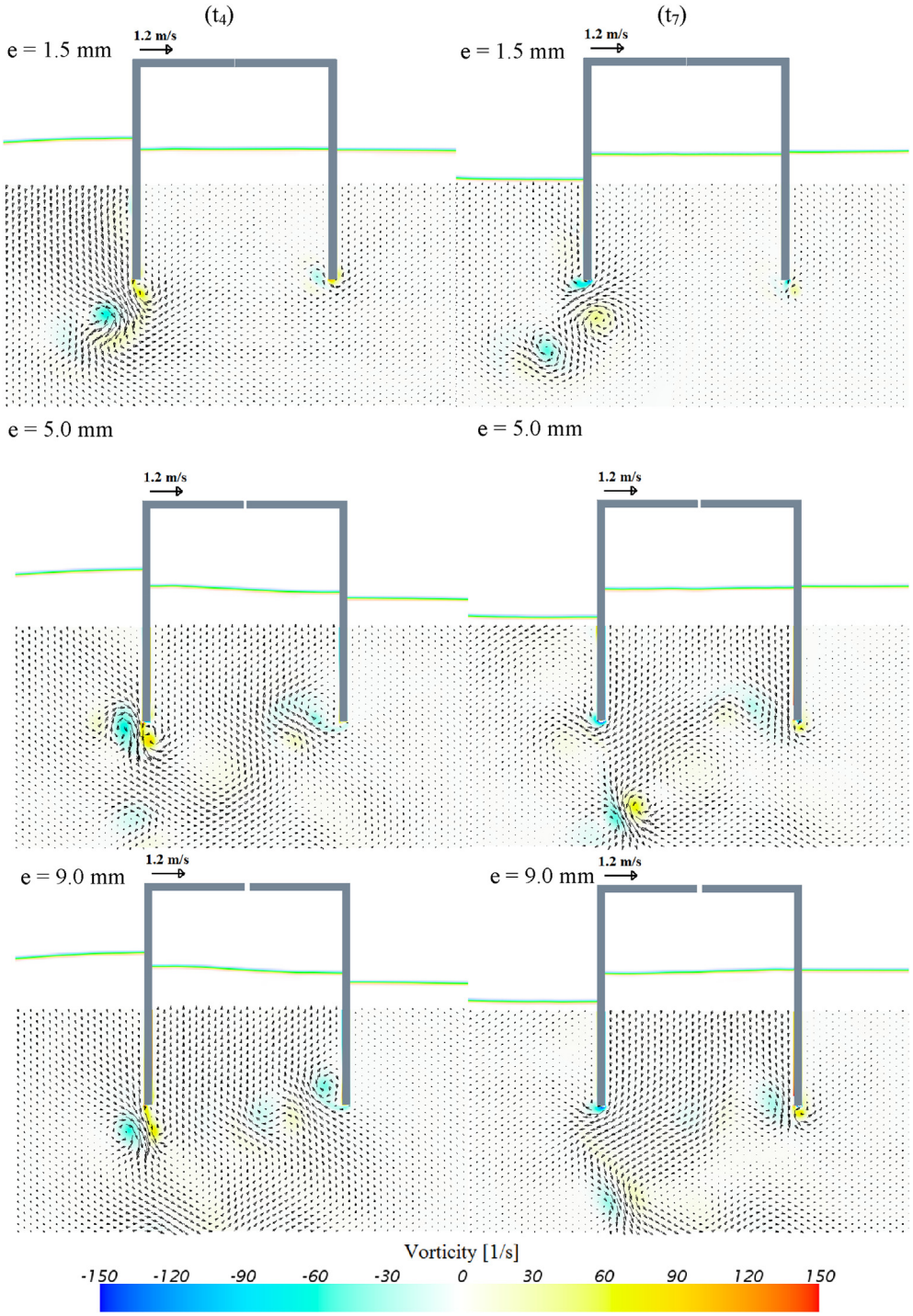

Fig. 21. PTO damping impact on the flow field for a constant 50 mm wave height and a wavelength of Kb = 0.8384.

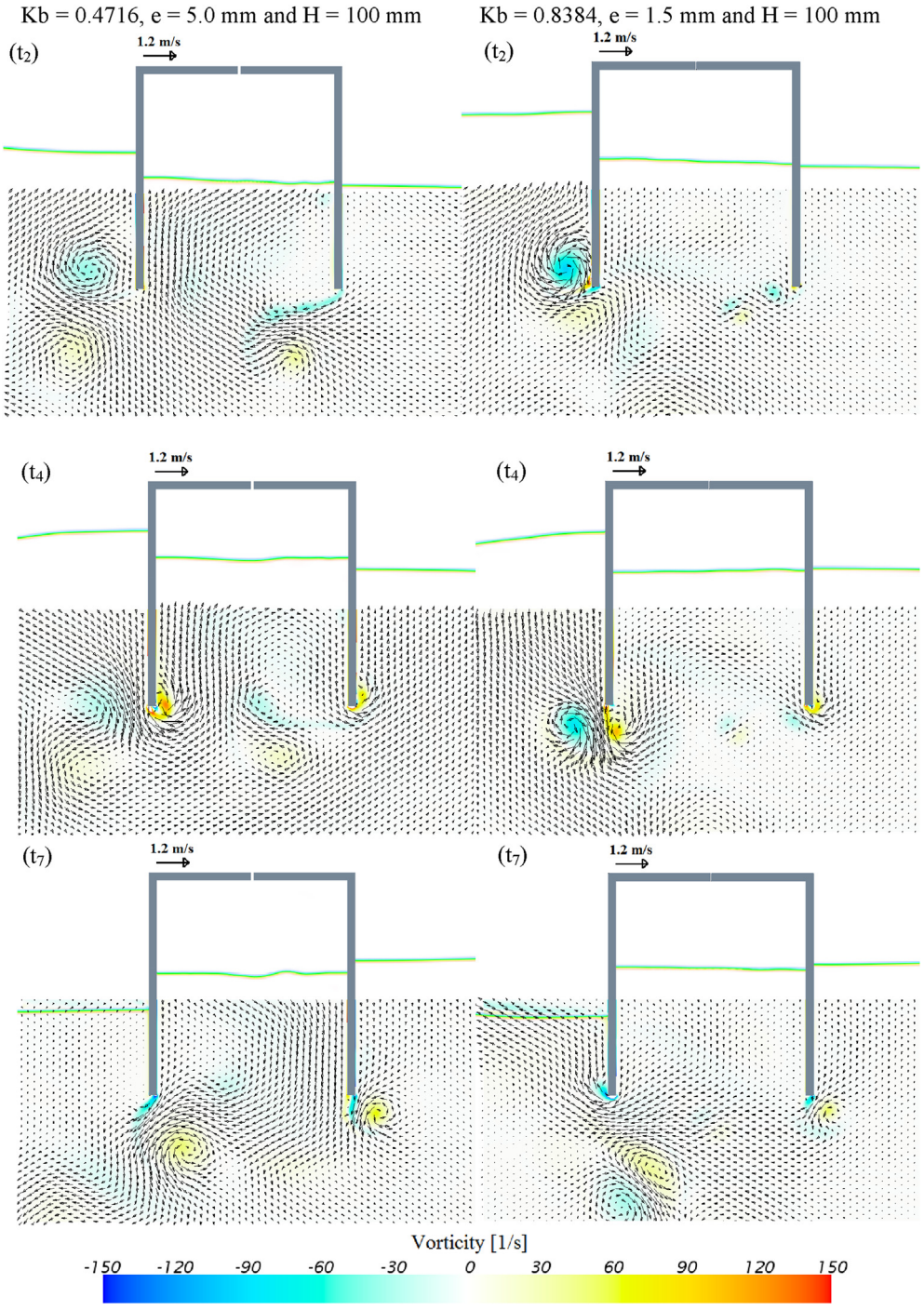

Fig. 22. Wave height (H = 100 mm) impact on the flow field. (left): Kb = 0.4716 and e = 5.0 mm, (right): Kb = 0.8384 and e = 1.5 mm.

sizes observed for the intermediate damping of e = 5.0 mm, whereas, at the rear wall, vortices become stronger as the PTO damping decreases. On the other side, during the outflow process, stronger vortices are observed at the seawall and lee wall under the highest and lowest applied damping, accordingly. Furthermore, decreasing the PTO damping induces more free surface nonlinearity and sloshing phenomena.

Regarding the incoming wave height impact, Fig. 22 discovers the consequences of increasing the wave height during the chamber filling and emptying processes. Two different conditions under a wave height of 100 mm are studied for wavelengths corresponding to Kb = 0.4716 with a damping e = 5.0 mm and Kb = 0.8384 under a damping e = 1.5 mm. In comparison with the results for 50 mm wave height shown in Figs. 18 and 19 for Kb = 0.4716, and e = 5.0 mm and Fig. 21 for Kb = 0.8384 and e = 1.5 mm, it was found that increasing the incoming wave height from 50 mm to 100 mm leads to amplifying the vortices magnitudes and enlarging their sizes throughout the whole operation process. Also, as a result of increasing the incident wave height, nonlinearity in the free

surface was observed especially under the lower pneumatic damping where the free surface looks to be highly distorted. Finally, in comparison with the 50 mm wave height, the significant increase in the vortices strength and size for Kb = 0.4716 and e = 5.0 mm under H = 100 mm, shown in Fig. 22 (left), supports the increase in the energy losses magnitude from doubling the wave height in the energy balance analysis shown in Fig. 17.

7. Conclusions

A 2D CFD model based on RANS–VOF is developed and applied in this paper in order to carry out wave energy balance analysis for an offshore floating–stationary oscillating water column–wave energy converter (OWC–WEC). The model was validated in good agreement with two sets of experimental measurements. The first included the chamber differential air pressure, chamber free surface elevation and device overall hydrodynamic efficiency over a wide range of wave frequencies, whereas the second validation was regarding the reflection, transmitted, losses and pressure coefficients. The comprehensively validated model allowed many parameters affecting the OWC wave energy conversion process such the incident wavelength, wave amplitude and the turbine pneumatic damping to be investigated. From the investigations carried out through a total of 102 numerical tests, the following conclusions are drawn:

7.1. Impact of the incoming wavelength

- The overall hydrodynamic efficiency, energy absorption coefficient, chamber air pressure and airflow rate increase with decreasing incident wavelength, achieve a maximum value at a certain wavelength, and then decline with a further decrease in the wavelength. Exception is found under the largest pneumatic damping where the pressure and airflow rate oscillation amplitudes tend to keep reducing as the wavelength decreases.
- Uneven power extraction between the inhalation and exhalation stages. The shorter the wavelength, the larger overall efficiency during inhalation process and vice versa.
- The reflection coefficient increases as the wavelength decreases, while the transmission coefficient, chamber free surface amplification factor and energy stored coefficient decrease as the wavelength becomes shorter.
- The losses coefficient accumulates with decreasing wavelength, reaches a stable/steady band region with small variations before increasing with a further increase in the wave steepness.
- The internal energy extraction coefficient has an inverse trend to the losses coefficient.
- Changing the incoming wavelength affects not only the vortices magnitude or size but also the rotational direction especially during the outflow stage at the front wall.
- As the wavelength reduces, the vortices generated at the rear wall become weak and almost invisible under high–frequency waves.
- Increasing the wave frequency introduces nonlinearity to the chamber free surface, and water sloshing becomes obvious.

7.2. Impact of the PTO pneumatic damping

- Increasing the PTO damping results in higher chamber differential air pressure, lower airflow rate, lesser chamber's free surface oscillation and smaller energy storage coefficient.
- The overall hydrodynamic efficiency increases as the PTO damping increases till hitting maxima and then drops down with a further increase in the damping.
- Altering the PTO damping can provide a damping value that tunes the device to a given wavelength, which provides an important control parameter for harvesting more energy over a wider frequency band.
- Asymmetric power extraction between the inflow and outflow processes. The larger the PTO damping, the higher overall efficiency during outflow process and vice versa.
- The internal energy extraction coefficient also increases as the damping increase till a certain value, and then a slight reduction is observed at higher damping factors.
- Similar to the wavelength effect, the losses coefficient has a contrary trend to that found for the internal energy extraction coefficient.
- The reflection and transmission coefficients are slightly rising and declining, accordingly when the applied damping increases.
- The more increase in the damping, the less energy stored coefficient with lesser impacts at higher damping values.
- The absorbed energy coefficient falls down with increasing the damping, except for the longer waves where this coefficient gradually increases as damping increases.
- The lower PTO damping applied on the chamber free surface, the stronger vortices generation especially at the rear side, whereas the higher damping leads to stronger vortices at the front walls during outflow.
- Chamber free surface waviness and sloshing are increasing as the adapted damping decreases.

7.3. Impact of the incoming wave height

- Increasing the incident wave height results in accumulating additional differential air pressure, and airflow rate, whereas the chamber's free surface amplification factor, as well as the energy storage coefficient, declines with increasing wave height.
- The unsymmetrical power extraction during the compression and decompression processes increases as the wave height increases.
- The reflection coefficient increases, while transmission coefficient and the energy absorption coefficient degrade with increasing wave height. An exception is found for the longer waves where the absorption coefficient tends to increase as the wave height grows up especially for low damping factors.

- The overall hydrodynamic efficiency is seen to decrease as the wave height increases. This impact becomes obvious when applying larger pneumatic damping. On the other hand, under small damping factors, there is a slight increase in the hydrodynamic efficiency. An exception is observed for the longer waves, which provide higher efficiency when the wave height increases especially under small and intermediate PTO damping; this provides a possibility for extracting more energy over a wider frequency band at more energetic seas.
- As the wave height moves up, the losses coefficient decreases and the internal energy extraction coefficient extends except for the intermediate wavelength.
- The generated vortices significantly strengthen as the incoming wave height arises. Similarly, the chamber free surface deformation and sloshing boost with increasing the wave height.

As a continuation of this research, the CFD model will be employed for further investigating the impact of adjusting the underwater geometry, especially the symmetrical and asymmetrical lips' submergence and its relevance to the incoming wave height. Furthermore, extending the current model to 3D will provide more insight into the device performance considering the impact of disturbing the flow by the chamber' sidewalls as well as the wave diffraction. Additionally, air compressibility may impact device performance, especially for large–scale prototypes (Falcão and Henriques, 2014), thus scaling effects with both incompressible and compressible airflow will be investigated.

References

Baudry, V., Babarit, A., Clement, A., 2013. An overview of analytical, numerical and experimental methods for modelling oscillating water columns. In: 10th European Wave and Tidal Energy Conference (EWTEC), September 2–5, Aalborg, Denmark.

CD-Adapco, 2015. User Guide STAR-CCM+ Version 10.02.

Choi, J., Yoon, S.B., 2009. Numerical simulations using momentum source wavemaker applied to RANS equation model. Coast. Eng. 56 (10), 1043–1060.

Crema, I., Simonetti, I., Cappietti, L., Oumeraci, H., 2015. Laboratory experiments on oscillating water column wave energy converters integrated in a very large floating structure. In: 11th European Wave and Tidal Energy Conference (EWTEC), September 6-11, Nantes, France.

Dalrymple, R.A., Dean, R.G., 1991. Water Wave Mechanics for Engineers and Scientists. World Scientific Publishing Company, New Jersey.

Drew, B., Plummer, A., Sahinkaya, M.N., 2009. A review of wave energy converter technology. Proceedings of the Institution of Mechanical Engineers. Part A J. Power Energy 223 (8), 887–902.

Elhanafi, A., Fleming, A., Leong, Z., Macfarlane, G., 2016a. Effect of RANS-based turbulence models on nonlinear wave generation in a two-phase numerical wave tank. Prog. Comput. Fluid Dyn. (in press).

Elhanafi, A., Fleming, A., MacFarlane, G., Leong, Z., 2016b. Numerical energy balance analysis for an onshore oscillating water column wave energy converter. Energy (provisionally accepted).

Evans, D., 1978. The oscillating water column wave-energy device. IMA J. Appl. Math. 22 (4), 423–433.

Evans, D., 1982. Wave-power absorption by systems of oscillating surface pressure distributions. J. Fluid Mech. 114, 481–499.

Evans, D., Porter, R., 1995. Hydrodynamic characteristics of an oscillating water column device. Appl. Ocean Res. 17 (3), 155–164.

Falcão, A.F., Henriques, J.C., 2014. Model-prototype similarity of oscillating-water-column wave energy converters. Int. J. Mar. Energy 6, 18–34.

Falcão, A.F., Henriques, J.C., 2015. Oscillating-water-column wave energy converters and air turbines: a review. Renew. Energy 85, 1391–1424.

Falcão, A.d.O., Sarmento, A., 1980. Wave generation by a periodic surface pressure and its application in wave-energy extraction. In: 15th International Congress of Theoretical and Applied Mechanics, Toronto, Canada.

Falnes, J., McIver, P., 1985. Surface wave interactions with systems of oscillating bodies and pressure distributions. Appl. Ocean Res. 7 (4), 225–234.

Fleming, A., Penesis, I., Goldsworthy, L., Macfarlane, G., Bose, N., Denniss, T., 2011. Phase averaged flow analysis in an oscillating water column wave energy converter. In: ASME, 30th International Conference on Ocean, Offshore and Arctic Engineering, Rotterdam, The Netherlands, June 19–24, pp. 475–484.

Fleming, A., Penesis, I., Macfarlane, G., Bose, N., Denniss, T., 2012a. Energy balance analysis for an oscillating water column wave energy converter. Ocean. Eng. 54, 26–33.

Fleming, A., Penesis, I., Macfarlane, G., Bose, N., Hunter, S., 2012b. Phase averaging of the velocity fields in an oscillating water column using splines. Proc. Inst. Mech. Eng. Part M J. Eng. Marit. Environ. 226 (4), 335–345, 1475090212439826.

Fleming, A., Penesis, I., Goldsworthy, L., Macfarlane, G., Bose, N., Denniss, T., 2013. Phase averaged flow analysis in an oscillating water column wave energy converter. J. Offshore Mech. Arct. Eng. 135 (2), 021901.

Goda, Y., Suzuki, T., 1976. Estimation of incident and reflected waves in random wave experiments. Coast. Eng. Proc. 1 (15).

Graw, K.-U., Schimmels, S., Lengricht, J., 2000. Quantifying Losses Around the Lip of an OWC by Use of Particle Image Velocimetry (PIV). LACER-Leipzig Annual Civil Engineering Report, Aalborg, Denmark.

He, F., Huang, Z., 2014. Hydrodynamic performance of pile-supported OWC-type structures as breakwaters: an experimental study. Ocean. Eng. 88, 618–626.

He, F., Huang, Z., Law, A.W.-K., 2012. Hydrodynamic performance of a rectangular floating breakwater with and without pneumatic chambers: an experimental study. Ocean. Eng. 51, 16–27.

He, F., Huang, Z., Law, A.W.-K., 2013. An experimental study of a floating breakwater with asymmetric pneumatic chambers for wave energy extraction. Appl. Energy 106, 222–231.

Hirt, C.W., Nichols, B.D., 1981. Volume of fluid (VOF) method for the dynamics of free boundaries. J. Comput. Phys. 39 (1), 201–225.

Hong, D., Hong, S., Hong, S., 2004. Numerical study of the motions and drift force of a floating OWC device. Ocean. Eng. 31 (2), 139–164.

Hong, K., Shin, S.-H., Hong, D.-C., Choi, H.-S., Hong, S.-W., 2007. Effects of shape parameters of OWC chamber in wave energy absorption. In: The Seventeenth International Offshore and Polar Engineering Conference, (ISOPE), Lisbon, Portugal, July 1-6, pp. 428–433.

Iturrioz, A., et al., 2014. Time-domain modeling of a fixed detached oscillating water column towards a floating multi-chamber device. Ocean. Eng. 76, 65–74.

Iturrioz, A., Guanche, R., Lara, J., Vidal, C., Losada, I., 2015. Validation of OpenFOAM® for oscillating water column three-dimensional modeling. Ocean. Eng. 107, 222–236.

Kamath, A., Bihs, H., Arntsen, Ø.A., 2015a. Numerical investigations of the hydrodynamics of an oscillating water column device. Ocean. Eng. 102, 40–50.

Kamath, A., Bihs, H., Arntsen, Ø.A., 2015b. Numerical modeling of power take-off damping in an oscillating water column device. Int. J. Mar. Energy 10, 1–16.

López, I., Pereiras, B., Castro, F., Iglesias, G., 2014. Optimisation of turbine-induced damping for an OWC wave energy converter using a RANS–VOF numerical model. Appl. Energy 127, 105–114.

López, I., Castro, A., Iglesias, G., 2015. Hydrodynamic performance of an oscillating water column wave energy converter by means of particle imaging velocimetry. Energy 83, 89–103.

López, I., Pereiras, B., Castro, F., Iglesias, G., 2016. Holistic performance analysis and turbine-induced damping for an OWC wave energy converter. Renew. Energy 85, 1155–1163.

Luo, Y., Nader, J.-R., Cooper, P., Zhu, S.-P., 2014. Nonlinear 2d analysis of the efficiency of fixed oscillating water column wave energy converters. Renew. Energy 64, 255–265.

Mansard, E.P., Funke, E., 1980. The measurement of incident and reflected spectra using a least squares method. Coast. Eng. Proc. 1 (17).

Mendes, A., Monteiro, W., 2007. Performance analysis of a model of OWC energy converter in non-linear waves. In: 7th European Wave and Tidal Energy Conference (EWTEC), September 11–13, Porto, Portugal.

Morris-Thomas, M.T., Irvin, R.J., Thiagarajan, K.P., 2007. An investigation into the hydrodynamic efficiency of an oscillating water column. J. Offshore Mech. Arct. Eng. 129 (4), 273–278.

Morrison, I.G., 1995. The Hydrodynamic Performance of an Oscillating Water Column Wave Energy Converter.

Müller, G., Whittaker, T.J., 1995. Visualisation of flow conditions inside a shoreline wave power-station. Ocean. Eng. 22 (6), 629–641.

Ning, D.-Z., Shi, J., Zou, Q.-P., Teng, B., 2015. Investigation of hydrodynamic performance of an OWC (oscillating water column) wave energy device using a fully nonlinear HOBEM (higher-order boundary element method). Energy 83, 177–188.

Ning, D.-Z., Wang, R.-Q., Zou, Q.-P., Teng, B., 2016. An experimental investigation of hydrodynamics of a fixed OWC wave energy converter. Appl. Energy 168, 636–648.

Sarmento, A., 1992. Wave flume experiments on two-dimensional oscillating water column wave energy devices. Exp. Fluids 12 (4–5), 286–292.

Sarmento, A.J., Falcão, A.d.O., 1985. Wave generation by an oscillating surface-pressure and its application in wave-energy extraction. J. Fluid Mech. 150, 467–485.

Sheng, W., Alcorn, R., Lewis, T., 2014. Numerical assessment on primary wave energy conversion of oscillating water columns. (OMAE2014–23218). In: ASME 2014 33rd International Conference on Ocean, Offshore and Arctic Engineering, San Francisco, USA, June 8–13.

Simonetti, I., Cappietti, L., El Safti, H., Oumeraci, H., 2015. Numerical modelling of fixed oscillating water column wave energy conversion devices: toward geometry hydraulic optimization. (OMAE2015-42056). In: ASME 2015 34th International Conference on Ocean, Offshore and Arctic Engineering, St. John's, Newfoundland, Canada, May 31–June 5.

Teixeira, P.R., Davyt, D.P., Didier, E., Ramalhais, R., 2013. Numerical simulation of an oscillating water column device using a code based on navier–stokes equations. Energy 61, 513–530.

Thíebaut, F., Pascal, R.e, Andreu, A.G.a., 2015. Investigation into the calibration of orifices used in OWC tank testing. In: 11th European Wave and Tidal Energy Conference (EWTEC), September 6–11, Nantes, France.

Tseng, R.-S., Wu, R.-H., Huang, C.-C., 2000. Model study of a shoreline wave-power system. Ocean. Eng. 27 (8), 801–821.

Zhang, Y., Zou, Q.-P., Greaves, D., 2012. Air–water two-phase flow modelling of hydrodynamic performance of an oscillating water column device. Renew. Energy 41, 159–170.